

# Mean States and Future Projections of Precipitation Over the Monsoon Transitional Zone in China in CMIP5 and CMIP6 Models

**Jinling Piao**

Institute of Atmospheric Physics Chinese Academy of Sciences

**Wen Chen** (✉ [cw@post.iap.ac.cn](mailto:cw@post.iap.ac.cn))

Institute of Atmospheric Physics Chinese Academy of Sciences <https://orcid.org/0000-0001-9327-9079>

**Shangfeng Chen**

Institute of Atmospheric Physics Chinese Academy of Sciences

**Hainan Gong**

Institute of Atmospheric Physics Chinese Academy of Sciences

**Lin Wang**

Institute of Atmospheric Physics Chinese Academy of Sciences

---

## Research Article

**Keywords:** Monsoon transitional zone, Precipitation projection, CMIP5, CMIP6, Moisture budget analysis

**Posted Date:** March 5th, 2021

**DOI:** <https://doi.org/10.21203/rs.3.rs-222416/v1>

**License:**  This work is licensed under a Creative Commons Attribution 4.0 International License.

[Read Full License](#)

---

**Version of Record:** A version of this preprint was published at Climatic Change on December 1st, 2021. See the published version at <https://doi.org/10.1007/s10584-021-03286-8>.

1 **Mean states and future projections of precipitation over the monsoon transitional zone in China in**  
2 **CMIP5 and CMIP6 models**

3  
4 Jinling Piao<sup>1</sup>·Wen Chen<sup>1,2\*</sup>·Shangfeng Chen<sup>1,2</sup>·Hainan Gong<sup>1,2</sup>·Lin Wang<sup>3,2</sup>

5 *<sup>1</sup>Center for Monsoon System Research, Institute of Atmospheric Physics, Chinese Academy of Sciences,*  
6 *Beijing 100190, China*

7 *<sup>2</sup>College of Earth and Planetary Sciences, University of Chinese Academy of Sciences, Beijing 100049,*  
8 *China*

9 *<sup>3</sup>Key Laboratory of Regional Climate-Environment for Temperate East Asia, Institute of Atmospheric*  
10 *Physics, Chinese Academy of Sciences, Beijing 100029, China*

11  
12 Submitted to *Climatic Change*

13 Submitted on February 9, 2021

14  
15 Corresponding author\*:

16 Wen Chen

17 Institute of Atmospheric Physics

18 Chinese Academy of Sciences

19 Beijing 100190, China

20 e-mail: cw@post.iap.ac.cn

## Abstract

The mean states and future projections of precipitation over the monsoon transitional zone (MTZ) in China are examined based on the historical and climate change projection simulations from phase 5 and phase 6 of the Coupled Model Intercomparison Project (CMIP5 and CMIP6, respectively). Ensemble means of CMIP6 models exhibit a clear improvement in capturing the annual mean and seasonal cycle of the precipitation over the MTZ, both in its spatial pattern and magnitude, compared to the counterparts of CMIP5 models. In addition, both CMIP5&6 models project a significant increase in the annual total precipitation amount and annual precipitation range, but with slightly stronger changes in CMIP6. For the climatological mean precipitation amount, the two versions' model ensembles show high consistency in the substantial role played by local evaporation in the supply of moisture in both the present-day and future-projection scenarios, with little contribution from the horizontal and vertical advection of moisture. The precipitation amount is projected to increase in all seasons, but with the strongest signals in summer. An analysis of the moisture budget indicates that the increase in summer precipitation is mainly due to evaporation and vertical moisture advection changes in both CMIP5&6 models. However, the change in vertical moisture advection in CMIP5 is primarily attributable to the thermodynamic effects associated with the humidity changes. By contrast, the dynamic effects induced by the atmospheric circulation changes play a dominant role for CMIP6, which is likely related to the stronger warming gradient between the mid-high latitudes and the tropics.

**Keywords:** Monsoon transitional zone · Precipitation projection · CMIP5 · CMIP6 · Moisture budget analysis

## 1 Introduction

The monsoon transitional zone in China (MTZ) is a southwest–northeast-oriented belt between arid and humid climate zones, with the monsoon area to its southeast and non-monsoon area to its northwest (Qian et al. 2007; Qian et al. 2012; Wang et al. 2017; Zhao et al. 2019; Zhao et al. 2020). This region is especially sensitive and vulnerable to climate change, frequently suffering from severe natural disasters (Piao et al. 2017; Wang et al. 2017). Far from oceanic water vapor sources, the annual total precipitation amount here is rather low, ranging from approximately 200 to 800 mm year<sup>-1</sup>, but presents a large interannual variation owing to the combined impacts of the East Asian summer monsoon (EASM) and mid-latitude westerly winds (Wu et al. 2003; Qian et al. 2009; Gao et al. 2014; Piao et al. 2018). Precipitation changes are of crucial importance because of the profound impacts they have on various aspects, such as vegetation cover (Lee et al. 2002; Mu et al. 2013), dust-storm occurrence (Liu et al. 2004; Lee and Sohn 2011), and drought frequency (Sato et al. 2007; Wang and He 2015), thereby posing a substantial threat to the ecological stability and sustainable development of the region. Huang et al. (2016) suggested that, by the end of this century, dryland areas will occupy half of the global land surface, resulting from enhanced regional warming via the reduced carbon sequestration. Considering the particular sensitivity of the MTZ region to climate change, understanding to what extent and how the precipitation here will respond to global warming is fundamentally important for projecting regional climate trends in the future.

Previous studies have suggested that the climatological mean precipitation amount over the MTZ region relies mainly on the water vapor supplied by local evaporation (Simmonds et al. 1999; Piao et al. 2018; Piao et al. 2020b), while interannual and interdecadal variations of precipitation are mainly due to changes in the water vapor transported by the large-scale atmospheric circulations (Zhou and Yu 2005; Hu et al. 2018; Piao et al. 2020a). For the climatological mean, local evaporation is regarded as the essential factor of influence for the input of moisture, as determined through analysis of the atmospheric water vapor budget, thus highlighting

63 the prominent bearing that land processes have on the regional hydrological cycle (Simmonds et al. 1999; Piao  
64 et al. 2018; Piao et al. 2020b). In terms of interannual and interdecadal variations, large-scale water vapor  
65 transport plays the most important role, which is controlled by the dynamic effects associated with circulation  
66 changes, rather than the thermodynamic effects related to the humidity changes (Hu et al. 2018; Piao et al.  
67 2020a). Given the particular location over the northern marginal area of the EASM system, the circulation  
68 changes here are subject not only to the EASM (Sun et al. 2007; Qian et al. 2012; Wang and He 2015), but  
69 also the mid-latitude westerly winds (Fukutomi et al. 2003; Fujinami et al. 2016; Piao et al. 2017).

70 In terms of the possible future changes in dry–wet conditions under global warming, a widely mentioned  
71 concept is the “wet gets wetter and dry gets drier” trend (Allen and Ingram 2002; Neelin et al. 2006; Allan and  
72 Soden 2007; Wentz et al. 2007; Chou and Lan 2012). Some studies have attributed this trend to thermodynamic  
73 effects, which, put simply, is that with the increased water vapor induced by global warming, the upward  
74 (downward) motion favors a precipitation increase (decrease) via the inducement of anomalous moisture  
75 convergence (divergence) over the wet (dry) regions, where ascending (descending) motions play the  
76 dominant role for the climatological mean (Chou and Neelin 2004; Held and Soden 2006; Chou et al. 2009;  
77 Zhang et al. 2019b). By comparison, dynamic effects are relatively less robust and more complicated, and  
78 exhibit large spread among different climate models in terms of their impacts on the precipitation changes  
79 (Chou et al. 2009). For instance, Jiang et al. (2020) indicated that the summer precipitation over Central Asia  
80 presents a drying trend in the coming century, which is closely associated with the decreased vertical moisture  
81 advection attributed to thermodynamic effects.

82 Several studies have been carried out to investigate projections of future climate over the MTZ region  
83 (Wentz et al. 2007; Wang and Chen 2014). Zhang et al. (2019a) pointed out that the climate types influence  
84 the response of surface evapotranspiration to global warming, and the type with annual total precipitation in  
85 the range of 250–300 mm shows the most significant sensitivity. Owing to the increased evaporation under

86 global warming, it is assumed that drought conditions over the MTZ region will be more severe compared to  
87 the present day, in spite of the remarkable increase in precipitation (Wang and Chen 2014; Wang et al. 2017).  
88 This remarkable increase in precipitation has been widely mentioned in previous studies (Liu et al. 2010; Chen  
89 and Frauenfeld 2014; Bao et al. 2015; Liu et al. 2017), accompanied by a more frequent occurrence and  
90 intensification of extreme events (Zhang et al. 2006; Zou and Zhou 2013; Zhou et al. 2014; Wang et al. 2017).

91 Despite the considerable progress and achievements in this research field, few studies have thus far  
92 focused on the physical mechanisms responsible for the increase in precipitation over the MTZ region. Key  
93 questions remain unanswered, such as: What are the changes in the corresponding hydrological components,  
94 such as local evaporation and water vapor transport? And what are the relative roles played by dynamic and  
95 thermodynamic effects? Besides, most of the above-mentioned studies on precipitation change were based on  
96 CMIP5 (phase 5 of the Coupled Model Intercomparison Project) simulation results (Taylor et al. 2012), and  
97 we now have at our disposal the outputs from the improved climate models participating in phase 6 of CMIP  
98 (i.e., CMIP6), which are expected to provide more reliable climate projections under different emission  
99 scenarios (Eyring et al. 2016). Accordingly, in this study, based on the model outputs of both CMIP5 and  
100 CMIP6, we attempt to elucidate the future changes in the components of the hydrological cycle over the MTZ  
101 region, especially the precipitation, and the underlying physical mechanisms involved. The data and methods  
102 employed in the study are introduced in section 2. In section 3, we evaluate the performances of the CMIP5  
103 and CMIP6 models in simulating the hydrological cycle. Future projections of precipitation over the MTZ and  
104 the responsible physical mechanisms are examined in section 4. Finally, conclusions and some further  
105 discussion are presented in section 5.

## 107 **2 Data and methods**

### 108 **2.1 Data**

109 In this study, 30 CMIP5 and 16 CMIP6 models (Table 1) are used with respect to the variables involved  
110 in calculating the hydrological components of interest. The first run of each model is used. The CMIP5 and  
111 CMIP6 future climate projection simulations are driven by a set of future climate scenarios based on the  
112 Representative Concentration Pathways (RCPs) (Van Vuuren et al. 2011) after 2005 in CMIP5 and the Shared  
113 Socioeconomic Pathways (SSPs) (Riahi et al. 2017) after 2014 in CMIP6. The RCP-based and SSP-based  
114 scenarios contain slight differences in their emission trajectories and land-use changes, while nominal forcing  
115 levels in the two scenarios reach approximately the same radiative forcing in 2100 (O'Neill et al. 2016). Hence,  
116 the climate projections based on the two scenarios following a similar forcing pathway are considered to be  
117 comparable, though not totally identical. The historical simulations in CMIP5 and CMIP6 are employed to  
118 represent the current climate, and the future projections based on the RCP8.5 and SSP5-8.5 forcing scenarios  
119 are employed to represent the future climate. To define the MTZ region, two monthly precipitation datasets  
120 are adopted: the Global Precipitation Climatology Project (GPCP), with a horizontal resolution of  $2.5^\circ \times 2.5^\circ$   
121 (Adler et al. 2003); and NOAA's Precipitation Reconstruction over Land (PRECL), with a horizontal  
122 resolution of  $1^\circ \times 1^\circ$  (Chen et al. 2002). For the purpose of evaluating the effects of model performance on  
123 the hydrological cycle, we further use the evaporation dataset provided by the land surface model estimates  
124 from GLDAS/NOAH at a horizontal resolution of  $0.25^\circ \times 0.25^\circ$  (Sheffield et al. 2006), and the specific  
125 humidity, surface pressure, and horizontal and vertical velocity derived from the European Centre for Medium-  
126 Range Weather Forecasts (ECMWF) Interim Re-Analysis (ERA-Interim), with a horizontal resolution of  
127  $1.5^\circ \times 1.5^\circ$  (Dee et al. 2011). All the datasets employed are interpolated onto the same horizontal resolution  
128 of  $1^\circ \times 1^\circ$  using the bilinear interpolation method to calculate the multi-model ensemble mean, pattern  
129 correlation, and pattern standard deviation. Four main research periods are chosen: 'present-day' (1979–2005),  
130 'near-term' (2021–2040), 'mid-term' (2041–2060), and 'long-term' (2081–2100).

## 131 **2.2 Methods**

### 2.2.1 Definition of the MTZ region

The MTZ region is selected based on the method in Zhao et al. (2019), which refers to the range of the monsoon domain boundaries over China. The monsoon domains are where the climatological mean precipitation differences between boreal summer [i.e., May–September (MJJAS)-averaged] and winter [i.e., November–March (NDJFM)-averaged] exceed  $2 \text{ mm day}^{-1}$ , and the summer precipitation amount accounts for more than 50% of the annual total (Liu et al. 2009). Precipitation differences are obtained using both the PRECL and GPCP datasets, and their 7-year running mean is further calculated to achieve the monsoon domain borders during 1979–2005 (Fig. 1). Then, as pointed out by Qian et al. (2007), the MTZ region over China is represented as the range of the monsoon domain borders. The GPCP and PRECL data are similar in terms of the resulting selection of the monsoon domain borders, albeit with a relatively broader scope produced by the latter (Fig. 1b). For convenience, their overlapping part is defined as the MTZ domain in this study, which is characterized by a southwest–northeast belt that includes parts of North and Northeast China (red box in Fig. 1). This chosen domain is closely consistent with that presented in previous studies using different criteria (Qian et al. 2007; Qian et al. 2009; Wang et al. 2017), indicating that our selection of the MTZ region is reasonable and reliable.

### 2.2.2 Water vapor budget

Following Schmitz and Mullen (1996), the balance equation for atmospheric water vapor can be expressed as

$$\frac{\partial W}{\partial t} = -\nabla \cdot \mathbf{Q} + E - P, \quad (1)$$

where  $E$  and  $P$  denote evaporation and precipitation, respectively.  $W$  represents total precipitable water, which can be calculated by

$$W = -\frac{1}{g} \int_{p_{\text{surf}}}^{p_{\text{top}}} q dp, \quad (2)$$

154 where  $p_{\text{top}}$  and  $p_{\text{surf}}$  are the pressure at the top of the troposphere and the surface, respectively;  $q$  represents the  
 155 specific humidity; and  $g$  is the gravitational acceleration.  $\mathbf{Q}$  and  $-\nabla \cdot \mathbf{Q}$  stand for the vertically integrated  
 156 water vapor flux and its convergence, which can be obtained by

$$157 \quad \mathbf{Q} = -\frac{1}{g} \int_{p_{\text{surf}}}^{p_{\text{top}}} \mathbf{V} q dp - \frac{1}{g} \int_{p_{\text{surf}}}^{p_{\text{top}}} \omega q dp \quad (3)$$

$$-\nabla \cdot \mathbf{Q} = -\nabla_{\text{h}} \cdot \mathbf{Q} - \nabla_{\text{p}} \cdot \mathbf{Q} = -\frac{1}{g} \int_{p_{\text{surf}}}^{p_{\text{top}}} \mathbf{V} \cdot \nabla_{\text{h}} q dp - \frac{1}{g} \int_{p_{\text{surf}}}^{p_{\text{top}}} \omega \cdot \nabla_{\text{p}} q dp ,$$

158 in which  $\mathbf{V}$  and  $\omega$  are the horizontal and vertical wind velocity, respectively; and  $-\nabla_{\text{h}} \cdot \mathbf{Q}$  and  $-\nabla_{\text{p}} \cdot \mathbf{Q}$  are  
 159 representative of the horizontal and vertical water vapor advection, respectively. Considering that the  $W$   
 160 tendency term always presents rather small changes ( $\frac{\partial W}{\partial t}$ ) compared to other terms, the atmospheric water

161 vapor budget changes can be expressed as

$$162 \quad \begin{aligned} P' &= E' + (-\nabla \cdot \mathbf{Q})' \\ &= E' + (-\nabla_{\text{h}} \cdot \mathbf{Q})' + (-\nabla_{\text{v}} \cdot \mathbf{Q})' \\ &= E' - \frac{1}{g} \int_{p_{\text{surf}}}^{p_{\text{top}}} (\mathbf{V} \cdot \nabla_{\text{h}} q)' dp - \frac{1}{g} \int_{p_{\text{surf}}}^{p_{\text{top}}} (\omega \cdot \nabla_{\text{p}} q)' dp , \end{aligned} \quad (4)$$

163 where ‘’ denotes the monthly deviation from the climatology.  $(-\nabla_{\text{h}} \cdot \mathbf{Q})'$  and  $(-\nabla_{\text{v}} \cdot \mathbf{Q})'$  can be further  
 164 decomposed as

$$165 \quad \begin{aligned} (-\nabla_{\text{h}} \cdot \mathbf{Q})' &= -\frac{1}{g} \int_{p_{\text{surf}}}^{p_{\text{top}}} (\mathbf{V} \cdot \nabla_{\text{h}} q)' dp = -\frac{1}{g} \int_{p_{\text{surf}}}^{p_{\text{top}}} \overline{\mathbf{V}} \cdot \nabla_{\text{h}} q' dp - \frac{1}{g} \int_{p_{\text{surf}}}^{p_{\text{top}}} \mathbf{V}' \cdot \nabla_{\text{h}} \overline{q} dp - \frac{1}{g} \int_{p_{\text{surf}}}^{p_{\text{top}}} \mathbf{V}' \cdot \nabla_{\text{h}} q' dp \\ (-\nabla_{\text{p}} \cdot \mathbf{Q})' &= -\frac{1}{g} \int_{p_{\text{surf}}}^{p_{\text{top}}} (\omega \cdot \nabla_{\text{p}} q)' dp = -\frac{1}{g} \int_{p_{\text{surf}}}^{p_{\text{top}}} \overline{\omega} \cdot \nabla_{\text{p}} q' dp - \frac{1}{g} \int_{p_{\text{surf}}}^{p_{\text{top}}} \omega' \cdot \nabla_{\text{p}} \overline{q} dp - \frac{1}{g} \int_{p_{\text{surf}}}^{p_{\text{top}}} \omega' \cdot \nabla_{\text{p}} q' dp , \end{aligned} \quad (5)$$

166 in both of which the overbar denotes the climatology for the present day. The first and second terms on the  
 167 right-hand side represent the thermodynamic effects associated with changes in the water vapor caused by the  
 168 temperature changes, and dynamic effects related to the circulation changes, respectively. The last term  
 169 represents the contribution from nonlinear processes.

### 170 2.2.3 Model skill score

171 To evaluate the performance of CMIP5 and CMIP6 models in simulating the climatological mean  
172 precipitation field, we employ the model skill score proposed by Taylor (2001), which is expressed as

$$173 \quad S = \frac{(1 + R)^2}{\left(\text{SDR} + \frac{1}{\text{SDR}}\right)^2}, \quad (6)$$

174 where  $R$  indicates the pattern correlation between the simulations and observations, and SDR denotes the ratio  
175 of the spatial standard deviation of model results to that of the observations.

### 176

## 177 **3 Evaluation of model performance in simulating the climatological mean precipitation**

### 178 **3.1 Climatological mean annual total precipitation field**

179 In the observation, the annual total precipitation over the MTZ region ranges from 200 to 600 mm,  
180 exhibiting a southeast–northwest-oriented structure (Fig. 2a). The multimodel ensemble (MME) means of the  
181 CMIP5 and CMIP6 models can simulate well the observed spatial distribution of climatological mean  
182 precipitation over the MTZ, but overestimate the precipitation amount (Figs. 2b, c). The overestimated amount  
183 for CMIP6 is approximately 193.9 and 104.7 mm over the southern and northern parts of the MTZ,  
184 respectively (Fig. 2e), which are much smaller than the corresponding values of 290.3 and 152.5 for CMIP5  
185 (Fig. 2d). This suggests that the CMIP6 models offer an improvement in reproducing the climatological mean  
186 precipitation over the MTZ as compared to the CMIP5 models (Fig. 2f).

187 The Taylor diagram is further utilized to give an intuitive perspective of model performance with respect  
188 to climatological mean precipitation over the MTZ region. Consistent with that seen in Fig. 2, the CMIP6  
189 models show much weaker intermodel diversity compared to their CMIP5 counterparts. Both CMIP5 and  
190 CMIP6 generally have larger standard deviations of the precipitation pattern, with half of the models showing  
191 values twice that of the observation for the former, but only a few for the latter (Figs. 3a, c). The pattern  
192 correlations are larger than 0.8 in nearly 50% of the CMIP6 models. However, only 23% (7 models) of the

193 CMIP5 models show a pattern correlation larger than 0.8. It is clear that the CMIP6 MME performs better  
194 both in terms of the pattern correlation and pattern standard deviation compared to that of CMIP5 (Figs. 3a,  
195 c). In addition, all the CMIP6 models except CanESM5, CESM2-WACCM and NorESM2-LM have skill  
196 scores that exceed 0.5, and four of them hold relatively high scores of beyond 0.8. As for the CMIP5 models,  
197 only half (14 models) of the models show skill scores larger than 0.5, and three models present relatively high  
198 skill scores (Figs. 3b, d). In terms of the MME, the skill score for CMIP6 is 0.74, which is higher than that in  
199 CMIP5 (0.6). The above results collectively suggest that CMIP6 models are relatively more skillful at  
200 simulating the climatological mean annual total precipitation over the MTZ region compared to the CMIP5  
201 models.

### 202 **3.2 Climatological mean annual cycle of the precipitation**

203 Over the MTZ region, summertime rainfall accounts for nearly 50% of the annual total precipitation (Piao  
204 et al. 2017). In contrast, there is only a small amount of rainfall in the winter season. Considering the striking  
205 contrast in the precipitation amount between the wet and dry seasons, it is worth investigating the possible  
206 future precipitation changes for each season. Hence, we further evaluate the model skill in simulating the  
207 climatological mean annual cycle of precipitation, along with other hydrological components (evaporation  
208 and moisture convergence) in the atmospheric water vapor balance equation, over the MTZ region. Both the  
209 CMIP5 and CMIP6 models are able to capture the general characteristics of the annual cycle of precipitation  
210 and evaporation, with maximum values in July and August and minimum values in the winter season (Fig. 4).  
211 Their simulated evaporation varies reasonably in-phase with that of the precipitation and acts as the main  
212 supply of moisture for precipitation throughout the year, which is consistent with observational evidence  
213 presented in previous studies (Piao et al. 2018). The MMEs of the CMIP5 and CMIP6 models can simulate  
214 the annual cycles of precipitation and evaporation well, but with slightly better performance for the latter,  
215 especially in the wet seasons (Fig. 4). Significant deviations exist in the simulated moisture convergence for

216 both model ensembles, with a large intermodel spread, in stark contrast to the precipitation and evaporation  
217 results. The residuals obtained from the CMIP5 and CMIP6 results account for approximately 10% of the  
218 precipitation amount in the summertime but 30% for the annual mean, indicating that the atmospheric water  
219 vapor budget is better closed in the summertime. In general, CMIP6 is more skillful at simulating the annual  
220 cycles of precipitation and evaporation compared to CMIP5, but fails to show clear improvement in  
221 reproducing the moisture convergence related to the large-scale water vapor transport.

#### 222

#### 223 **4 Future precipitation changes and the related physical mechanism**

224 The CMIP5 and CMIP6 models present quite similar features in their representation of the changes in  
225 annual total precipitation and annual precipitation range over the MTZ region throughout the 20th and 21st  
226 centuries, manifesting in a flat decreasing trend before the 1980s that turns into a sharp increasing trend  
227 thereafter (Figs. 5a, c). For the present-day simulations, the two MMEs exhibit reasonably in-phase evolutions.  
228 However, after the 2010s, their discrepancies become apparent, with the rate of increase shown by CMIP6  
229 seeming to be persistently larger than that of CMIP5 (Figs. 5a, c). Relative to the present-day climatology, the  
230 annual total precipitation amount in the CMIP5 MME median increases by about 2.8% (interquartile range:  
231 1.3%–6.1%) for the near-term, and up to 9.5% (5.4%–11.2%) and 18.3% (10.4–22.8%) for the mid-term and  
232 long-term, respectively (Fig. 5b). Considerable model spread still exists in CMIP6, and the MME median  
233 shows corresponding precipitation increases of 8.1%, 12.5% and 23.4%, all of which exceed those in CMIP5  
234 (Fig. 5b). The annual precipitation range also increases significantly, from 3.2%, 9.2% and 17.1% for the near-  
235 term, mid-term and long-term in CMIP5, to 8.0%, 14.2% and 21.5% in CMIP6 (Fig. 5d). The increase in the  
236 annual precipitation range in CMIP5 and CMIP6 can further lead to a strengthening of the seasonality from  
237 the perspective of the dry and wet conditions, exerting prominent impacts on the regional water cycle over the  
238 MTZ region. What, then, are the precipitation changes in each season and how much do they contribute to the

239 changes in the annual precipitation range? And what is the underlying physical mechanism for the precipitation  
240 changes?

241 Based on the balance equation for the atmospheric water vapor, the precipitation amount relies on the  
242 evaporation and the horizontal and vertical moisture advection. From the perspective of the climatological  
243 mean for the present-day and future periods, considerable model spread exists in the projections of all the  
244 hydrological components of interest in different seasons for both the CMIP5 and CMIP6 models (Fig. 6). The  
245 CMIP5 and CMIP6 models share several common features in their mean states of the atmospheric water vapor  
246 budget over the MTZ region: The precipitation amount is mostly accounted for by the summertime rainfall,  
247 and local evaporation appears to be the main source for the available water vapor during different future  
248 periods, consistent with the present-day climatology (Piao et al. 2018); plus, both the horizontal and vertical  
249 moisture advection are much smaller than the evaporation, exerting a limited or even a negative contribution  
250 to the climatological mean precipitation amount.

251 In terms of the future precipitation changes, the contributions of the related hydrological components  
252 differ greatly from those for the climatological mean. In both the CMIP5 and CMIP6 MMEs, the increase in  
253 evaporation and horizontal moisture advection together dominate the precipitation changes in winter and  
254 autumn, while the vertical moisture advection exerts negative impacts (Figs. 7a, b, g, h); in spring, the wetting  
255 trend is balanced by the increase in evaporation and decrease in horizontal and vertical moisture advection  
256 (Figs. 7c, d). For the summertime changes, quite different features can be identified (Figs. 7e, f). In sharp  
257 contrast to the decreasing trend shown in other seasons, the vertical moisture advection exhibits a prominent  
258 increase in all three future periods, with the increment amount close to that for local evaporation. The changes  
259 in horizontal moisture advection are relatively small and show distinctive differences between CMIP5 and  
260 CMIP6, with a weak increase (decrease) for the former (latter). In spite of the opposite changes in horizontal  
261 moisture advection between CMIP5 and CMIP6, the vertical moisture advection and local evaporation

262 together dominate the increase in precipitation for both MMEs. Besides, the increase in precipitation shows  
263 its most significant signals in summer, with the increment amount being 0.11 (0.25) mm day<sup>-1</sup>, 0.25 (0.44) mm  
264 day<sup>-1</sup> and 0.48 (0.56) mm day<sup>-1</sup> in the near-term, mid-term and long-term for the MME medians of CMIP5  
265 (CMIP6). Considering these distinctive features shown in summer, in the following we mainly focus on the  
266 future precipitation changes in the summer season, and discuss the related physical mechanism. It should be  
267 noted that all the hydrological components of interest present stronger changes in CMIP6 than those in CMIP5,  
268 which might be attributable to the more sensitive climate, as shown in previous studies (Fan et al. 2020; Flynn  
269 and Mauritsen 2020; Zelinka et al. 2020).

270 The corresponding spatial distributions are further displayed to examine if differences exist in the  
271 dominant factors of influence for the summertime increase in precipitation over different parts of the MTZ  
272 region. In the CMIP5 model simulations, the increase in precipitation is weak in the near-term, with significant  
273 signals limited to just a small area (Fig. 8a), which might be due to the large impacts of the internal variability.  
274 Alongside this, a significant increase in evaporation is noticeable over the northern and southern parts (Fig.  
275 8d). Both the horizontal and vertical moisture advection show weak changes (Figs. 8g, j). In the mid-term,  
276 both the precipitation and vertical moisture advection exhibit significant increases that are concentrated over  
277 the middle part (Figs. 8b, k), with a significant increase in evaporation but weak horizontal moisture advection  
278 over the whole domain (Figs. 8e, h). The changes in the long-term show quite similar features, but with the  
279 significant increase for both the precipitation and vertical moisture advection extending over a large part of  
280 the MTZ (Figs. 8c, l). This indicates that, for CMIP5, changes in the evaporation and vertical moisture  
281 advection are the dominant factors for the future increase in precipitation over most parts of the MTZ region,  
282 with little contribution from the horizontal moisture advection. In comparison, CMIP6 shows enhanced  
283 changes for all the hydrological components involved. Significant increases in precipitation occupy a large  
284 domain of the MTZ region for all three future periods (Figs. 9a, b, c), with the most significant changes situated

285 over the coastal area of East China. The future changes in evaporation are similar to those shown in CMIP5,  
286 with a significant increase covering most of the domain for all three future periods (Figs. 9d, e, f). Different  
287 from the domain-wide weak increase shown in CMIP5 (Figs. 8g, h, i), the CMIP6-simulated horizontal  
288 moisture advection presents a weak increase and decrease over the northern and southern parts, respectively.  
289 The increase in vertical moisture advection is remarkably strengthened in all three future periods for CMIP6,  
290 as compared to those simulated by CMIP5. The significant signals occupy the central part in the near-term but  
291 extend over most parts of the MTZ region in the mid-term and long-term (Figs. 9j, k, l), with the amplitude  
292 and spatial pattern quite similar to those corresponding to the increase in precipitation. Hence, the changes in  
293 evaporation and vertical moisture advection are considered as the two dominant factors for the future increase  
294 in precipitation over most parts of the MTZ region in both CMIP5 and CMIP6.

295 The above analysis indicates that vertical moisture advection plays an important role in the future increase  
296 in precipitation over the MTZ region. In the following, we further examine the factors contributing to the  
297 changes in vertical moisture advection, with a focus on the relative contributions of the dynamic and  
298 thermodynamic components. Accompanying the increase in vertical moisture advection in the three future  
299 periods in CMIP5, the thermodynamic component presents quite similar changes in terms of amplitude and  
300 spatial pattern, with relatively weak change in the near-term (Fig. 10d) but a strengthened and significant  
301 increase in the mid-term and long-term (Figs. 10e, f). From a quantitative perspective, the thermodynamic  
302 component can account for approximately 58%, 61% and 67% of the total vertical moisture advection changes  
303 for the MME median of CMIP5 in the near-term, mid-term and long-term, respectively (Fig. 11a). By contrast,  
304 the dynamic (Figs. 10a–c) and nonlinear (Figs. 10g–i) components exhibit weak and non-significant changes  
305 over the MTZ, exerting little impact compared to the thermodynamic component. This accords well with the  
306 ‘wet-getting-wetter’ mechanism. Climatologically, ascending motions occupy most parts of the MTZ region.  
307 With the increased atmospheric water vapor due to global warming, the thermodynamic effect, which is

308 dominated by the humidity changes, exhibits a significant increase, contributing to the projected increase in  
309 precipitation. In sharp contrast, the thermodynamic component shows no significant changes over the whole  
310 MTZ region for CMIP6 (Figs. 12d–f). Instead, the dynamic component experiences increasing changes in the  
311 three future periods (Figs. 12a–c), corresponding well to the significant changes in total vertical moisture  
312 advection (Figs. 9j–l). Besides, the nonlinear component can also exert considerable impacts, with significant  
313 changes recognizable over a large domain (Figs. 12g–i). In this case, the dynamic component turns out to be  
314 the dominant factor influencing the increase in vertical moisture advection in CMIP6, explaining 70%, 46%  
315 and 36% in the near-term, mid-term and long-term, respectively (Fig. 11b).

316 The intensities of the dynamic effects are determined by the changes in vertical motion. In CMIP5,  
317 significant changes in descending motion are noticeable over the southern and central parts of China, together  
318 with marked changes in ascending motion over small areas of Inner Mongolia. However, the changes in  
319 vertical motion over most parts of the MTZ are fairly weak (Figs. 13a–c), and this may contribute to the weak  
320 dynamic effects on the changes in vertical moisture advection (Figs. 10a–c). By contrast, pronounced changes  
321 in ascending motion are apparent over the MTZ, especially in its central part, in CMIP6 (Figs. 14a–c). This  
322 explains the important role played by the dynamic component in the vertical moisture advection changes (Figs.  
323 12a–c). The enhanced changes in ascending motion are assumed to be associated with the stronger warming  
324 gradient between the tropics and mid–high latitudes in CMIP6 (Figs. 14d–f), as compared to CMIP5 (Figs.  
325 13d–f). The significant warming in the mid–high latitudes has already been mentioned in previous studies  
326 (Feng et al. 2014; Fan et al. 2020), and the suggested reason for its increase in CMIP6 is the higher climate  
327 sensitivity (Fan et al. 2020; Flynn and Mauritsen 2020; Zelinka et al. 2020). The stronger warming gradient  
328 in CMIP6 induces a larger sea level pressure gradient between the tropics and mid–high latitudes, which favors  
329 a strengthening of the prevailing southerly winds over the eastern coast of East China and a weakening of the  
330 mid–high-latitude westerly winds (Figs. 14g–i). This further results in more significant changes in ascending

331 motion via intensified convergence over the MTZ in CMIP6 (Figs. 14g–i) than in CMIP5 (Figs. 13g–i).

## 333 **5 Conclusions**

334 This study begins by examining the performance of CMIP5 and CMIP6 models in capturing the  
335 climatological mean and seasonal cycle of the precipitation over the MTZ. Then, we examine future  
336 projections of precipitation over the MTZ based on future climate projection simulations of the CMIP5 and  
337 CMIP6 models. In terms of the climatological mean, the MMEs of CMIP5 and CMIP6 can successfully  
338 reproduce the southeast–northwest-oriented precipitation gradient, but overestimate the annual total  
339 precipitation amount over the whole domain. Compared to CMIP5, CMIP6 is more skillful at simulating the  
340 annual mean precipitation in terms of both amplitude and spatial pattern. From the perspective of the annual  
341 cycle, the CMIP5 and CMIP6 models are both able to reproduce the monthly evolution of precipitation and  
342 evaporation, but with slightly higher skill for the CMIP6 models, especially in summer.

343 Compared to the present-day climatology, the annual total amount and annual range for the precipitation  
344 exhibit a sharp increase until the end of the 21st century based on the CMIP5 (RCP8.5) and CMIP6 (SSP5-  
345 8.5) future-projection simulations. The two MMEs reveal that the increase in summertime precipitation  
346 dominates the intensified annual cycle, with limited contribution from the precipitation changes in the dry  
347 seasons. Considering that the annual total precipitation amount is mostly concentrated in summer, the  
348 enhanced annual cycle would strengthen the seasonality of wet and dry conditions, exerting substantial  
349 impacts on the regional water cycle. It should be noted that CMIP6 shows a larger amplitude of the increase  
350 in precipitation compared to CMIP5, indicating that the dry and wet conditions are more sensitive under the  
351 prescriptions of the CMIP6 model runs. From the perspective of the climatological mean, both CMIP5 and  
352 CMIP6 show that the future precipitation amount is mainly supplied by local evaporation, with little

353 contribution from horizontal and vertical moisture advection.

354 As for the future precipitation changes, the dominant factors of influence differ greatly among different  
355 seasons in CMIP5 and CMIP6. For winter and autumn, the increase in precipitation operates under the  
356 combined impacts of evaporation and horizontal moisture advection; whereas, in spring, the change in  
357 precipitation is balanced by the increase in evaporation and decrease in moisture advection. As for summer,  
358 the vertical moisture advection exhibits a significant increase with the amplitude close to that of the increase  
359 in evaporation, which is in stark contrast to the decreasing trend in other seasons. The horizontal moisture  
360 advection presents relatively small changes and shows opposite signals between CMIP5 and CMIP6, with  
361 weak increases over the whole domain for the former but strong decreases covering the southern part of the  
362 MTZ region for the latter. In this case, the changes in vertical moisture advection and local evaporation  
363 together dominate the summertime increase in precipitation. Further analysis reveals that the increase in  
364 vertical moisture advection is dominated by the thermodynamic component associated with humidity changes  
365 for CMIP5, but is mainly attributable to the dynamic effects related to circulation changes for CMIP6. The  
366 strengthened dynamic effects in CMIP6 are related to stronger vertical ascending motions, which may be  
367 associated with the increased warming gradient between the mid–high latitudes and the tropics.

## 369 **Declarations**

370  
371 **Funding** This study was supported jointly by the National Natural Science Foundation of China (Grants  
372 41721004, 41961144016 and 41875115), and the Jiangsu Collaborative Innovation Center for Climate Change.

373  
374 **Conflicts of interest** The authors declare that they have no competing interests.

376 **Availability of data and material** CMIP5 and CMIP6 datasets are publicly available on the website of Earth  
377 System Grid Federation (<https://esgf-index1.ceda.ac.uk/projects/esgf-ceda/>). Observational products are  
378 publicly available online via the following websites: ERA-Interim  
379 (<https://www.ecmwf.int/en/forecasts/datasets/reanalysis-datasets/era-interim>), GLDAS/NOAH  
380 (<https://disc.gsfc.nasa.gov/datasets?keywords=GLDAS>), PRECL and GPCP  
381 (<https://psl.noaa.gov/data/gridded/tables/precipitation.html>).

382

383 **Code availability** Figures in this study are constructed with the NCAR Command Language  
384 (<http://www.ncl.ucar.edu/>). All codes used in this study are available from the corresponding author.

385

386 **Authors' contributions** Wen Chen designed the research. Jinling Piao performed the analysis. Wen Chen,  
387 Jinling Piao and Shangfeng Chen wrote the paper. All authors discussed the results and commented on the  
388 manuscript.

389

390 **Ethics approval** Not applicable.

391

392 **Consent to participate** Not applicable.

393

394 **Consent for publication** Not applicable.

395 **References**

- 396 Adler RF, Huffman GJ, Chang A, Ferraro R, Xie P-P, Janowiak J, Rudolf B, Schneider U, Curtis S, Bolvin D  
397 (2003) The version-2 global precipitation climatology project (GPCP) monthly precipitation analysis  
398 (1979–present). *J Hydrometeorol* 4:1147-1167.
- 399 Allan RP, Soden BJ (2007) Large discrepancy between observed and simulated precipitation trends in the  
400 ascending and descending branches of the tropical circulation. *Geophys Res Lett* 34:L18705
- 401 Allen MR, Ingram WJ (2002) Constraints on future changes in climate and the hydrologic cycle. *Nature*  
402 419:228-232.
- 403 Bao J, Feng J, Wang Y (2015) Dynamical downscaling simulation and future projection of precipitation over  
404 China. *J Geophys Res* 120:8227-8243.
- 405 Chen L, Frauenfeld OW (2014) A comprehensive evaluation of precipitation simulations over China based on  
406 CMIP5 multimodel ensemble projections. *J Geophys Res* 119:5767-5786.
- 407 Chen M, Xie P, Janowiak JE, Arkin PA (2002) Global land precipitation: A 50-yr monthly analysis based on  
408 gauge observations. *J Hydrometeorol* 3:249-266.
- 409 Chou C, Lan C-W (2012) Changes in the annual range of precipitation under global warming. *J Clim* 25:222-  
410 235.
- 411 Chou C, Neelin JD (2004) Mechanisms of global warming impacts on regional tropical precipitation. *J Clim*  
412 17:2688-2701.
- 413 Chou C, Neelin JD, Chen C-A, Tu J-Y (2009) Evaluating the “rich-get-richer” mechanism in tropical  
414 precipitation change under global warming. *J Clim* 22:1982-2005.
- 415 Dee DP, Uppala SM, Simmons A, Berrisford P, Poli P, Kobayashi S, Andrae U, Balmaseda M, Balsamo G,  
416 Bauer dP (2011) The ERA-Interim reanalysis: Configuration and performance of the data assimilation  
417 system. *Quart J Roy Meteor Soc* 137:553-597.

418 Eyring V, Bony S, Meehl GA, Senior CA, Stevens B, Stouffer RJ, Taylor KE (2016) Overview of the Coupled  
419 Model Intercomparison Project Phase 6 (CMIP6) experimental design and organization. *Geosci Model*  
420 *Dev* 9:1937-1958.

421 Fan X, Duan Q, Shen C, Wu Y, Xing C (2020) Global surface air temperatures in CMIP6: historical  
422 performance and future changes. *Environ Res Lett* 15:104056.

423 Feng S, Hu Q, Huang W, Ho C-H, Li R, Tang Z (2014) Projected climate regime shift under future global  
424 warming from multi-model, multi-scenario CMIP5 simulations. *Global Planet Change* 112:41-52.

425 Flynn CM, Mauritsen T (2020) On the climate sensitivity and historical warming evolution in recent coupled  
426 model ensembles. *Atmos Chem Phys* 20:7829-7842.

427 Fujinami H, Yasunari T, Watanabe T (2016) Trend and interannual variation in summer precipitation in eastern  
428 Siberia in recent decades. *Int J Climatol* 36:355-368.

429 Fukutomi Y, Igarashi H, Masuda K, Yasunari T (2003) Interannual variability of summer water balance  
430 components in three major river basins of northern Eurasia. *J Hydrometeorol* 4:283-296.

431 Gao Z, Hu Z-Z, Jha B, Yang S, Zhu J, Shen B, Zhang R (2014) Variability and predictability of Northeast  
432 China climate during 1948–2012. *Clim Dyn* 43:787-804.

433 Held IM, Soden BJ (2006) Robust responses of the hydrological cycle to global warming. *J Clim* 19:5686-  
434 5699.

435 Hu P, Wang M, Yang L, Wang X, Feng G (2018) Water Vapor Transport Related to the Interdecadal Shift of  
436 Summer Precipitation over Northern East Asia in the Late 1990s. *J Meteorol Res* 32:781-793.

437 Huang J, Yu H, Guan X, Wang G, Guo R (2016) Accelerated dryland expansion under climate change. *Nat*  
438 *Clim Chang* 6:166-171.

439 Jiang J, Zhou T, Chen X, Zhang L (2020) Future changes in precipitation over Central Asia based on CMIP6  
440 projections. *Environ Res Lett* 15:054009.

- 441 Lee E-H, Sohn B-J (2011) Recent increasing trend in dust frequency over Mongolia and Inner Mongolia  
442 regions and its association with climate and surface condition change. *Atmos Environ* 45:4611-4616.
- 443 Lee R, Yu F, Price K, Ellis J, Shi P (2002) Evaluating vegetation phenological patterns in Inner Mongolia  
444 using NDVI time-series analysis. *Int J Remote Sens* 23:2505-2512.
- 445 Liu J, Du H, Wu Z, He HS, Wang L, Zong S (2017) Recent and future changes in the combination of annual  
446 temperature and precipitation throughout China. *Int J Climatol* 37:821-833.
- 447 Liu J, Wang B, Ding Q, Kuang X, Soon W, Zorita E (2009) Centennial variations of the global monsoon  
448 precipitation in the last millennium: results from ECHO-G model. *J Clim* 22:2356-2371.
- 449 Liu X, Yin ZY, Zhang X, Yang X (2004) Analyses of the spring dust storm frequency of northern China in  
450 relation to antecedent and concurrent wind, precipitation, vegetation, and soil moisture conditions. *J*  
451 *Geophys Res* 109:D16210
- 452 Liu Y, Li X, Zhang Q, Guo Y, Gao G, Wang J (2010) Simulation of regional temperature and precipitation in  
453 the past 50 years and the next 30 years over China. *Quat Int* 212:57-63.
- 454 Mu S, Yang H, Li J, Chen Y, Gang C, Zhou W, Ju W (2013) Spatio-temporal dynamics of vegetation coverage  
455 and its relationship with climate factors in Inner Mongolia, China. *J Geogr Sci* 23:231-246.
- 456 Neelin JD, Münnich M, Su H, Meyerson JE, Holloway CE (2006) Tropical drying trends in global warming  
457 models and observations. *Proc Natl Acad Sci USA* 103:6110-6115.
- 458 O'Neill BC, Tebaldi C, Van Vuuren DP, Eyring V, Friedlingstein P, Hurtt G, Knutti R, Kriegler E, Lamarque  
459 J-F, Lowe J (2016) The scenario model intercomparison project (ScenarioMIP) for CMIP6. *Geosci Model*  
460 *Dev* 9:3461-3482
- 461 Piao J, Chen W, Chen S (2020a) Water vapour transport changes associated with the interdecadal decrease in  
462 the summer rainfall over Northeast Asia around the late-1990s. *Int J Climatol*.
- 463 Piao J, Chen W, Chen S, Gong H, Zhang Q (2020b) Summer Water Vapor Sources in Northeast Asia and East

464 Siberia Revealed by a Moisture-Tracing Atmospheric Model. *J Clim* 33:3883-3899.

465 Piao J, Chen W, Wei K, Liu Y, Graf H-F, Ahn J-B, Pogoreltsev A (2017) An abrupt rainfall decrease over the  
466 Asian inland plateau region around 1999 and the possible underlying mechanism. *Adv Atmos Sci* 34:456-  
467 468.

468 Piao J, Chen W, Zhang Q, Hu P (2018) Comparison of moisture transport between Siberia and northeast Asia  
469 on annual and interannual time scales. *J Clim* 31:7645-7660.

470 Qian W, Ding T, Hu H, Lin X, Qin A (2009) An overview of dry-wet climate variability among monsoon-  
471 westerly regions and the monsoon northernmost marginal active zone in China. *Adv Atmos Sci* 26:630-  
472 641.

473 Qian W, Lin X, Zhu Y, Xu Y, Fu J (2007) Climatic regime shift and decadal anomalous events in China. *Clim*  
474 *Chang* 84:167-189.

475 Qian W, Shan X, Chen D, Zhu C, Zhu Y (2012) Droughts near the northern fringe of the East Asian summer  
476 monsoon in China during 1470–2003. *Clim Chang* 110:373-383.

477 Riahi K, Van Vuuren DP, Kriegler E, Edmonds J, O’neill BC, Fujimori S, Bauer N, Calvin K, Dellink R,  
478 Fricko O (2017) The shared socioeconomic pathways and their energy, land use, and greenhouse gas  
479 emissions implications: an overview. *Glob Environ Change* 42:153-168.

480 Sato T, Kimura F, Kitoh A (2007) Projection of global warming onto regional precipitation over Mongolia  
481 using a regional climate model. *J Hydrol* 333:144-154.

482 Schmitz JT, Mullen SL (1996) Water vapor transport associated with the summertime North American  
483 monsoon as depicted by ECMWF analyses. *J Clim* 9:1621-1634.

484 Sheffield J, Goteti G, Wood EF (2006) Development of a 50-year high-resolution global dataset of  
485 meteorological forcings for land surface modeling. *J Clim* 19:3088-3111.

486 Simmonds I, Bi D, Hope P (1999) Atmospheric water vapor flux and its association with rainfall over China in

487 summer. *J Clim* 12:1353-1367.

488 Sun L, Shen B, Gao Z, Sui B, Bai L, Wang S-H, An G, Li J (2007) The impacts of moisture transport of East  
489 Asian monsoon on summer precipitation in Northeast China. *Adv Atmos Sci* 24:606-618.

490 Taylor KE (2001) Summarizing multiple aspects of model performance in a single diagram. *J Geophys Res*  
491 106:7183-7192.

492 Taylor KE, Stouffer RJ, Meehl GA (2012) An overview of CMIP5 and the experiment design. *Bull Am*  
493 *Meteorol Soc* 93:485-498.

494 Van Vuuren DP, Edmonds J, Kainuma M, Riahi K, Thomson A, Hibbard K, Hurtt GC, Kram T, Krey V,  
495 Lamarque J-F (2011) The representative concentration pathways: an overview. *Clim Chang* 109:5-31.

496 Wang H, He S (2015) The north China/northeastern Asia severe summer drought in 2014. *J Clim* 28:6667-  
497 6681.

498 Wang L, Chen W (2014) A CMIP5 multimodel projection of future temperature, precipitation, and  
499 climatological drought in China. *Int J Climatol* 34:2059-2078.

500 Wang L, Chen W, Huang G, Zeng G (2017) Changes of the transitional climate zone in East Asia: past and  
501 future. *Clim Dyn* 49:1463-1477.

502 Wentz FJ, Ricciardulli L, Hilburn K, Mears C (2007) How much more rain will global warming bring? *Science*  
503 317:233-235.

504 Wu R, Hu Z-Z, Kirtman BP (2003) Evolution of ENSO-related rainfall anomalies in East Asia. *J Clim*  
505 16:3742-3758.

506 Zelinka MD, Myers TA, McCoy DT, Po-Chedley S, Caldwell PM, Ceppi P, Klein SA, Taylor KE (2020)  
507 Causes of higher climate sensitivity in CMIP6 models. *Geophys Res Lett* 47:e2019GL085782.

508 Zhang Q, Yang Z, Hao X, Yue P (2019a) Conversion features of evapotranspiration responding to climate  
509 warming in transitional climate regions in northern China. *Clim Dyn* 52:3891-3903.

510 Zhang W, Zhou T, Zhang L, Zou L (2019b) Future intensification of the water cycle with an enhanced annual  
511 cycle over global land monsoon regions. *J Clim* 32:5437-5452.

512 Zhang Y, Xu Y, Dong W, Cao L, Sparrow M (2006) A future climate scenario of regional changes in extreme  
513 climate events over China using the PRECIS climate model. *Geophys Res Lett* 33:L24702.

514 Zhao W, Chen S, Chen W, Yao S, Nath D, Yu B (2019) Interannual variations of the rainy season withdrawal  
515 of the monsoon transitional zone in China. *Clim Dyn* 53:2031-2046.

516 Zhao W, Chen W, Chen S, Yao SL, Nath D (2020) Combined impact of tropical central-eastern Pacific and  
517 North Atlantic sea surface temperature on precipitation variation in monsoon transitional zone over China  
518 during August–September. *Int J Climatol* 40:1316-1327.

519 Zhou B, Wen QH, Xu Y, Song L, Zhang X (2014) Projected Changes in Temperature and Precipitation  
520 Extremes in China by the CMIP5 Multimodel Ensembles. *J Clim* 27:6591-6611.

521 Zhou TJ, Yu RC (2005) Atmospheric water vapor transport associated with typical anomalous summer rainfall  
522 patterns in China. *J Geophys Res* 110:D08104.

523 Zou L, Zhou T (2013) Near future (2016-40) summer precipitation changes over China as projected by a  
524 regional climate model (RCM) under the RCP8.5 emissions scenario: Comparison between RCM  
525 downscaling and the driving GCM. *Adv Atmos Sci* 30:806-818.

## Figure Captions

**Fig. 1.** The 7-year running-mean precipitation differences equal to  $2 \text{ mm day}^{-1}$  between boreal summer (i.e., MJJAS-averaged) and winter (i.e., NDJFM-averaged) during 1979–2005 (blue lines). The red boxes in **a** and **b** represent the selected MTZ region.

**Fig. 2.** Mean annual total precipitation in the **a** GPCP, and the MME of **b** CMIP5 and **c** CMIP6 models over 1979–2005 (unit:  $\text{mm year}^{-1}$ ). Differences in the mean annual total precipitation between **d** the MME of CMIP5 and GPCP, **e** the MME of CMIP6 and GPCP, and **f** the MME of CMIP6 and CMIP5.

**Fig. 3.** Taylor diagrams (left-hand panels) and skill scores (right-hand panels) of the simulated precipitation over the MTZ region for the (**a**, **b**) CMIP5 and (**c**, **d**) CMIP6 models against the observations.

**Fig. 4.** The climatological mean annual cycle of precipitation (Pr), evaporation (Eva), vertically integrated moisture convergence (Moi\_con) and tendency of atmospheric precipitable water (dpw/dt) over the MTZ region obtained from ERA-Interim (lines with asterisks), the MME means (lines), and the 25th–75th percentile model intervals (shading) for the **a** CMIP5 and **b** CMIP6 ensembles (lines) (units:  $\text{mm month}^{-1}$ ).

**Fig. 5.** MME mean (lines) and the 25th–75th percentile model intervals (shading) for the 20-year running mean anomalies of the **a** annual total precipitation (unit:  $\text{mm year}^{-1}$ ) and **c** the annual precipitation range (unit:  $\text{mm day}^{-1}$ ) relative to the present-day climatology (1979–2005) over the MTZ region. Changes in the **b** annual total precipitation and **d** annual precipitation range (%) for the near-term (2021–2040), mid-term (2041–2060) and long-term (2081–2100) relative to the present-day (1979–2005) climatology for the CMIP5 (red) and

549 CMIP6 (blue) ensembles. Box-and-whisker plots present the 10th, 25th, 50th, 75th and 90th percentiles.

550

551 **Fig. 6.** Climatological mean amount of precipitation, evaporation, horizontal moisture advection ( $\langle v dq dh \rangle$ )  
552 and vertical moisture advection ( $\langle w dq dp \rangle$ ) in (a, b) winter, (c, d) spring, (e, f) summer and (g, h) autumn,  
553 for the present-day, near-term, mid-term and long-term derived from the CMIP5 (left-hand panels) and CMIP6  
554 (right-hand panels) model ensembles (units:  $\text{mm day}^{-1}$ ). Box-and-whisker plots present the 10th, 25th, 50th,  
555 75th and 90th percentiles.

556

557 **Fig. 7.** Changes in precipitation, evaporation, horizontal moisture convergence ( $\langle v dq dh \rangle$ ) and vertical  
558 moisture convergence ( $\langle w dq dp \rangle$ ) in (a, b) winter, (c, d) spring, (e, f) summer and (g, h) autumn in the near-  
559 term, mid-term and long-term relative to the present-day climatology derived from the CMIP5 (left-hand  
560 panels) and CMIP6 (right-hand panels) model ensembles (units:  $\text{mm day}^{-1}$ ). Box-and-whisker plots present  
561 the 10th, 25th, 50th, 75th and 90th percentiles.

562

563 **Fig. 8.** Changes in precipitation, evaporation, horizontal moisture advection ( $\langle v dq dh \rangle'$ ) and vertical moisture  
564 advection ( $\langle w dq dp \rangle'$ ) for the MME of CMIP5 models in the near-term (left-hand panels), mid-term (middle  
565 panels) and long-term (right-hand panels) under the RCP8.5 scenario compared to the present-day climatology  
566 (unit:  $\text{mm day}^{-1}$ ). The dotted area denotes that at least three quarters of modes share the same-sign changes.

567

568 **Fig. 9.** As in Fig. 8, but for the CMIP6 MME.

569

570 **Fig. 10.** The dynamic ( $\langle w' dq dp \rangle$ ), thermodynamic ( $\langle w (dq dp) \rangle$ ) and nonlinear ( $\langle w' (dq dp)' \rangle$ ) components  
571 of the changes in vertical moisture advection for CMIP5 MME in the near-term (left-hand panels), mid-term

572 (middle panels) and long-term (right-hand panels) under the RCP8.5 scenario compared to the present-day  
573 climatology (unit:  $\text{mm day}^{-1}$ ). The dotted areas denote that at least three quarters of models share same-sign  
574 changes.

575

576 **Fig. 11.** Changes in vertical moisture advection ( $-\langle w dqdp \rangle'$ ) and its dynamic ( $-\langle w' dqdp \rangle$ ), thermodynamic ( $-\langle w(dqdp)' \rangle$ ) and nonlinear ( $-\langle w'(dqdp)' \rangle$ ) components in the near-term, mid-term and long-term relative to  
577 the present-day climatology derived from the **a** CMIP5 and **b** CMIP6 model ensembles (unit:  $\text{mm day}^{-1}$ ). Box-  
578 and-whisker plots present the 10th, 25th, 50th, 75th and 90th percentiles.

580

581 **Fig. 12.** As in Fig. 10, but for the CMIP6 MME.

582

583 **Fig. 13.** Changes in vertical velocity at 500 hPa (unit:  $\text{Pa s}^{-1}$ ), surface air temperature (unit:  $^{\circ}\text{C}$ ), sea level  
584 pressure (unit: Pa) and horizontal wind at 850 hPa (unit:  $\text{m s}^{-1}$ ) for the CMIP5 MME in the near-term (left-  
585 hand panels), mid-term (middle panels) and long-term (right-hand panels) under the RCP8.5 scenario  
586 compared to the present-day climatology. The dotted areas denote that at least three quarters of models share  
587 same-sign changes.

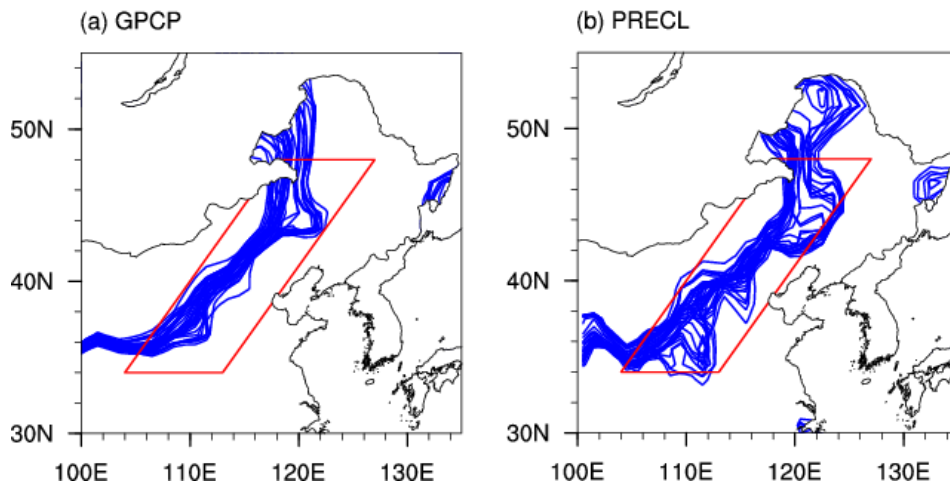
588

589 **Fig. 14.** As in Fig.13, but for the CMIP6 MME.

590 **Table 1.** Descriptions of the CMIP5 and CMIP6 models used in this study.

591

Sl. No.	CMIP5 Model Name	Resolution (in °)	Sl. No.	CMIP6 Model Name	Resolution
1	ACCESS1-0	1.88×1.25	1	ACCESS-CM2	100
2	ACCESS1-3	1.88×1.25	2	ACCESS-ESM1-5	250
3	bcc-csm1-1	2.81×2.79	3	AWI-CM-1-1-MR	100
4	BNU-ESM	2.81×2.79	4	BCC-CSM2-MR	250
5	CanESM2	2.81×2.79	5	CanESM5	500
6	CNRM-CM5	1.41×1.40	6	CESM2-WACCM	100
7	CSIRO-Mk3-6-0	1.88×1.87	7	FGOALS-f3-L	100
8	FGOALS-g2	2.81×2.79	8	GFDL-CM4	100
9	FGOALS-s2	2.81×1.66	9	INM-CM4-8	100
10	FIO-ESM	2.81×2.81	10	IPSL-CM6A-LR	250
11	GFDL-CM3	2.50×2.00	11	MIROC6	250
12	GFDL-ESM2G	2.00×2.02	12	MPI-ESM1-2-HR	100
13	GFDL-ESM2M	2.50×2.02	13	MPI-ESM1-2-LR	250
14	GISS-E2-H	2.50×2.00	14	MRI-ESM2-0	100
15	GISS-E2-H-CC	2.50×2.00	15	NorESM2-LM	250
16	GISS-E2-R	2.50×2.00	16	NorESM2-MM	100
17	GISS-E2-R-CC	2.50×2.00			
18	Inmcm4	2.00×1.50			
19	IPSL-CM5A-LR	3.75×1.89			
20	IPSL-CM5A-MR	2.50×1.27			
21	IPSL-CM5B-LR	3.75×1.89			
22	MIROC-ESM	2.81×2.79			
23	MIROC-ESM-CHEM	2.81×2.79			
24	MIROC5	1.41×1.40			
25	MPI-ESM-LR	1.88×1.87			
26	MPI-ESM-MR	1.88×1.87			
27	MRI-CGCM3	1.13×1.12			
28	MRI-ESM1	1.13×1.12			
29	NorESM1-M	2.50×1.89			
30	NorESM1-ME	2.50×1.89			



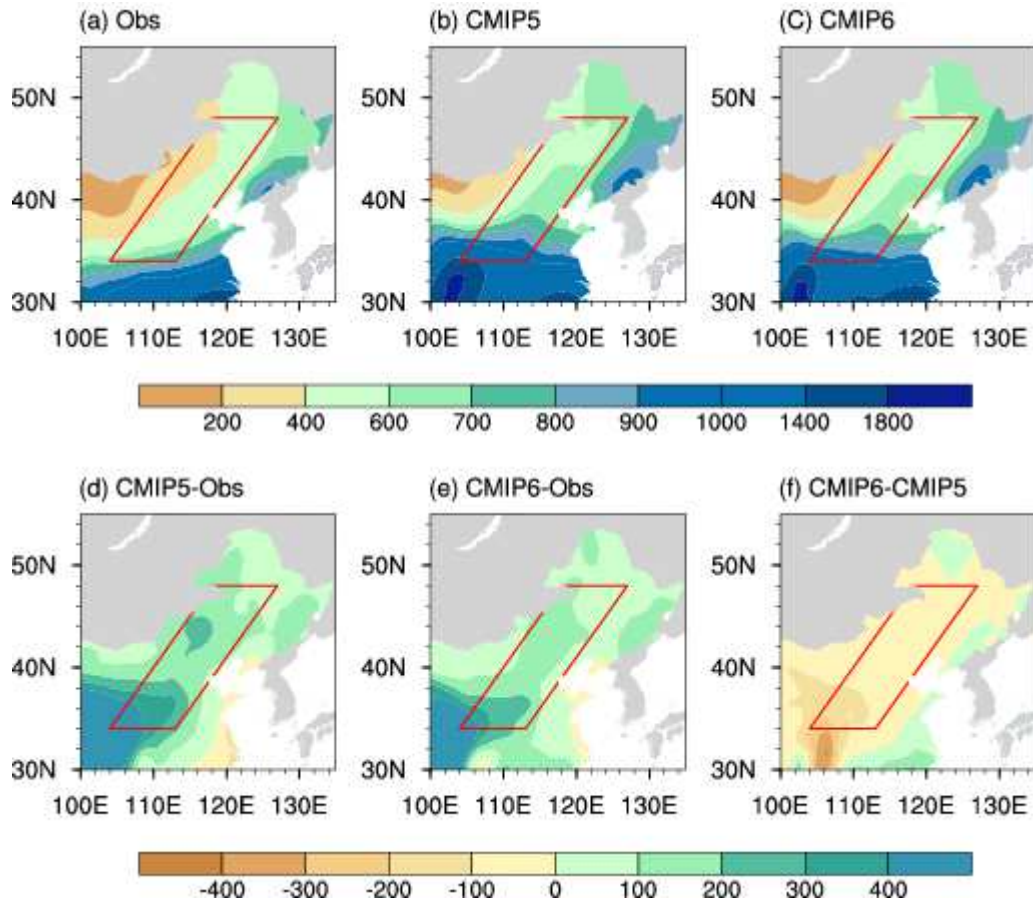
592

593

594

595

**Fig. 1.** The 7-year running-mean precipitation differences equal to 2 mm day<sup>-1</sup> between boreal summer (i.e., MJJAS-averaged) and winter (i.e., NDJFM-averaged) during 1979–2005 (blue lines). The red boxes in **a** and **b** represent the selected MTZ region.



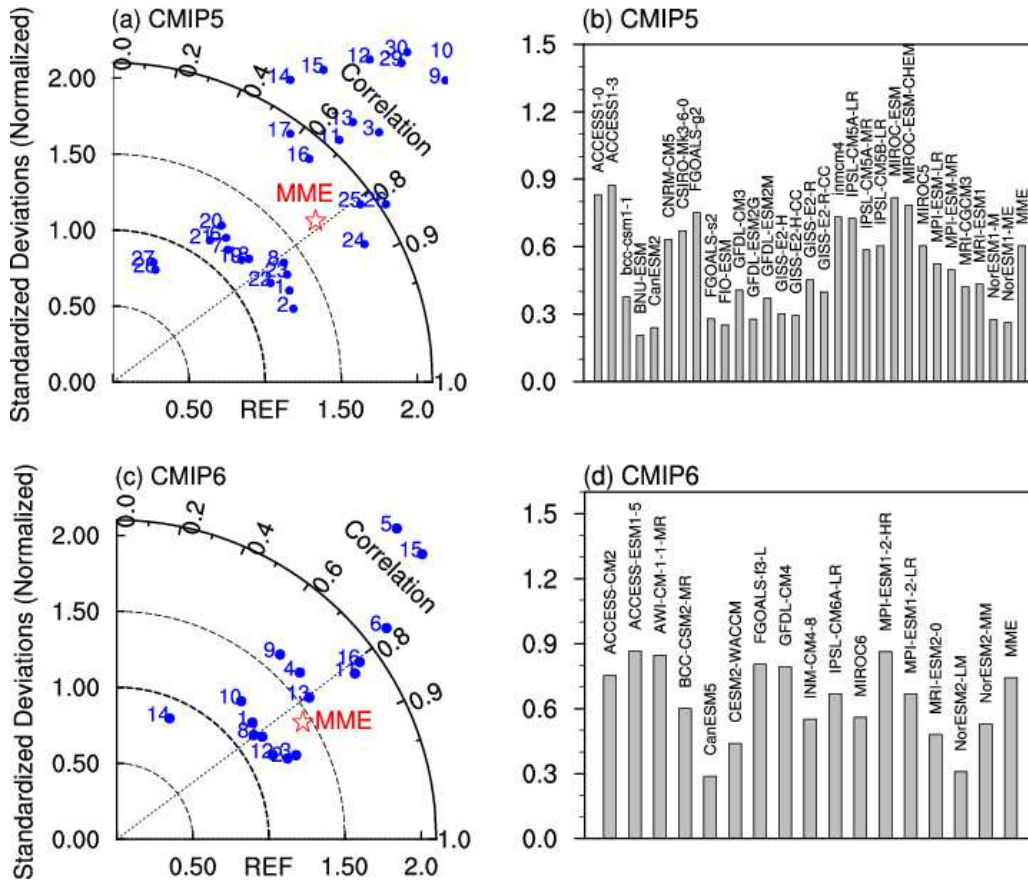
596

597

598

599

**Fig. 2.** Mean annual total precipitation in the **a** GPCP, and the MME of **b** CMIP5 and **c** CMIP6 models over 1979–2005 (unit: mm year<sup>-1</sup>). Differences in the mean annual total precipitation between **d** the MME of CMIP5 and GPCP, **e** the MME of CMIP6 and GPCP, and **f** the MME of CMIP6 and CMIP5.



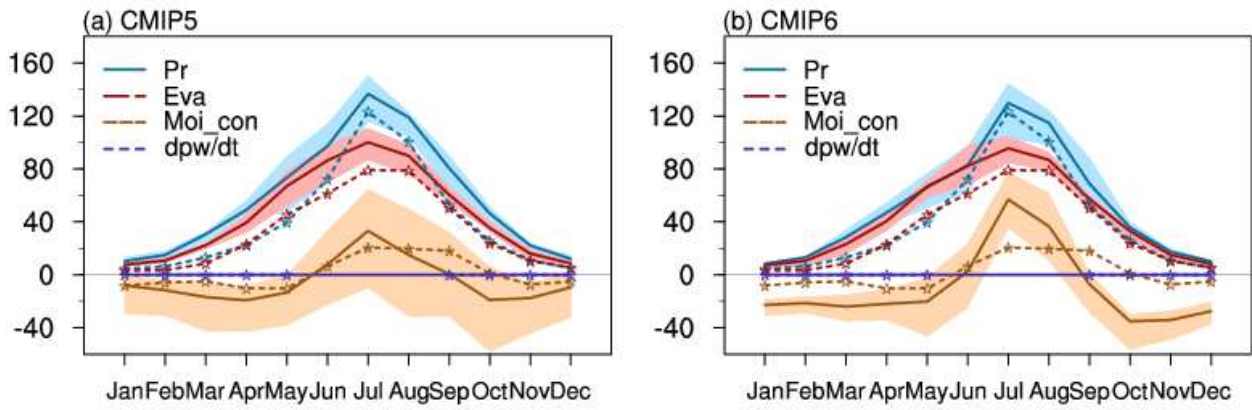
600

601

**Fig. 3.** Taylor diagrams (left-hand panels) and skill scores (right-hand panels) of the simulated precipitation

602

over the MTZ region for the (a, b) CMIP5 and (c, d) CMIP6 models against the observations.



603

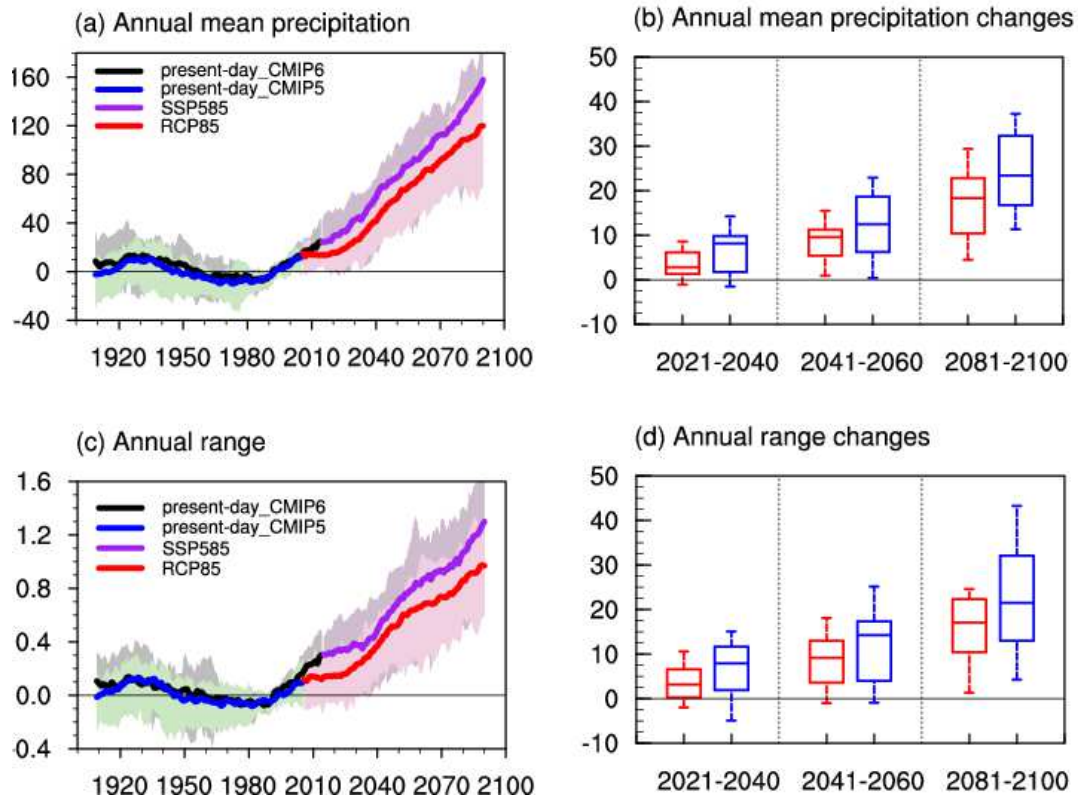
604

605

606

607

**Fig. 4.** The climatological mean annual cycle of precipitation (Pr), evaporation (Eva), vertically integrated moisture convergence (Moi\_con) and tendency of atmospheric precipitable water (dpw/dt) over the MTZ region obtained from ERA-Interim (lines with asterisks), the MME means (lines), and the 25th–75th percentile model intervals (shading) for the **a** CMIP5 and **b** CMIP6 ensembles (lines) (units:  $\text{mm month}^{-1}$ ).



608

609

610

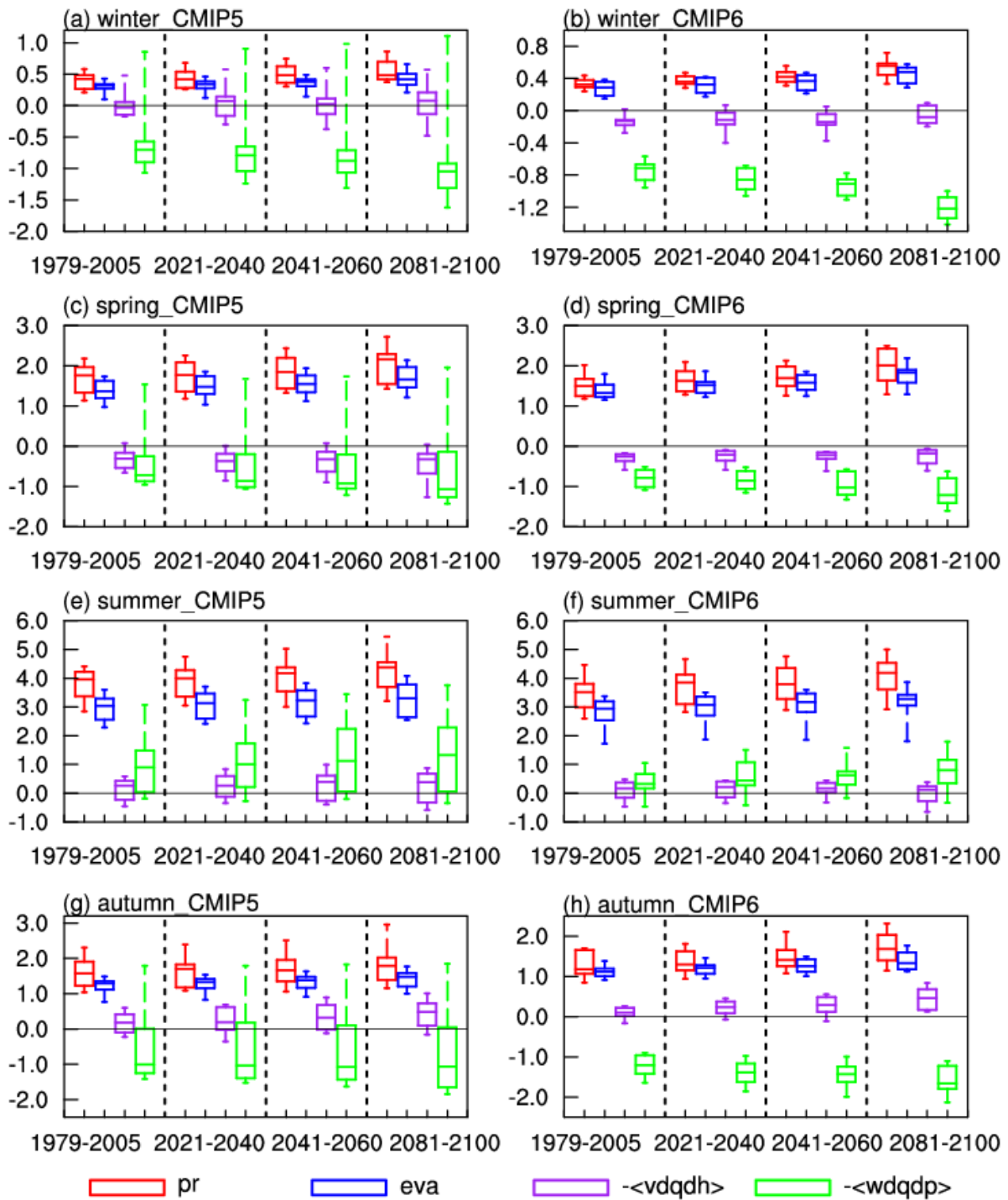
611

612

613

614

**Fig. 5.** MME mean (lines) and the 25th–75th percentile model intervals (shading) for the 20-year running mean anomalies of the **a** annual total precipitation (unit:  $\text{mm year}^{-1}$ ) and **c** the annual precipitation range (unit:  $\text{mm day}^{-1}$ ) relative to the present-day climatology (1979–2005) over the MTZ region. Changes in the **b** annual total precipitation and **d** annual precipitation range (%) for the near-term (2021–2040), mid-term (2041–2060) and long-term (2081–2100) relative to the present-day (1979–2005) climatology for the CMIP5 (red) and CMIP6 (blue) ensembles. Box-and-whisker plots present the 10th, 25th, 50th, 75th and 90th percentiles.



615

616

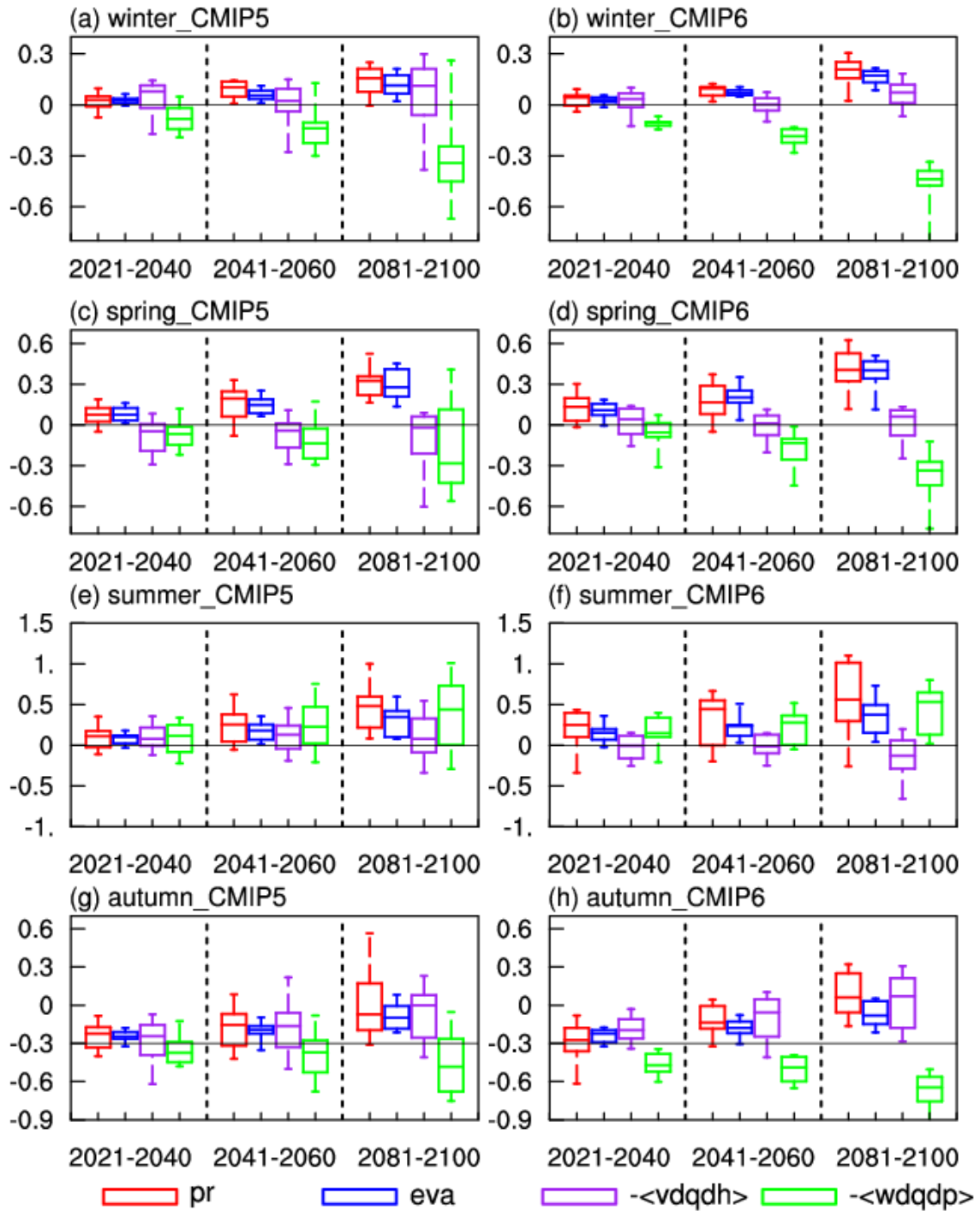
617

618

619

620

**Fig. 6.** Climatological mean amount of precipitation, evaporation, horizontal moisture advection ( $-\langle v dqdh \rangle$ ) and vertical moisture advection ( $-\langle w dqdp \rangle$ ) in (a, b) winter, (c, d) spring, (e, f) summer and (g, h) autumn, for the present-day, near-term, mid-term and long-term derived from the CMIP5 (left-hand panels) and CMIP6 (right-hand panels) model ensembles (units:  $\text{mm day}^{-1}$ ). Box-and-whisker plots present the 10th, 25th, 50th, 75th and 90th percentiles.



621

622

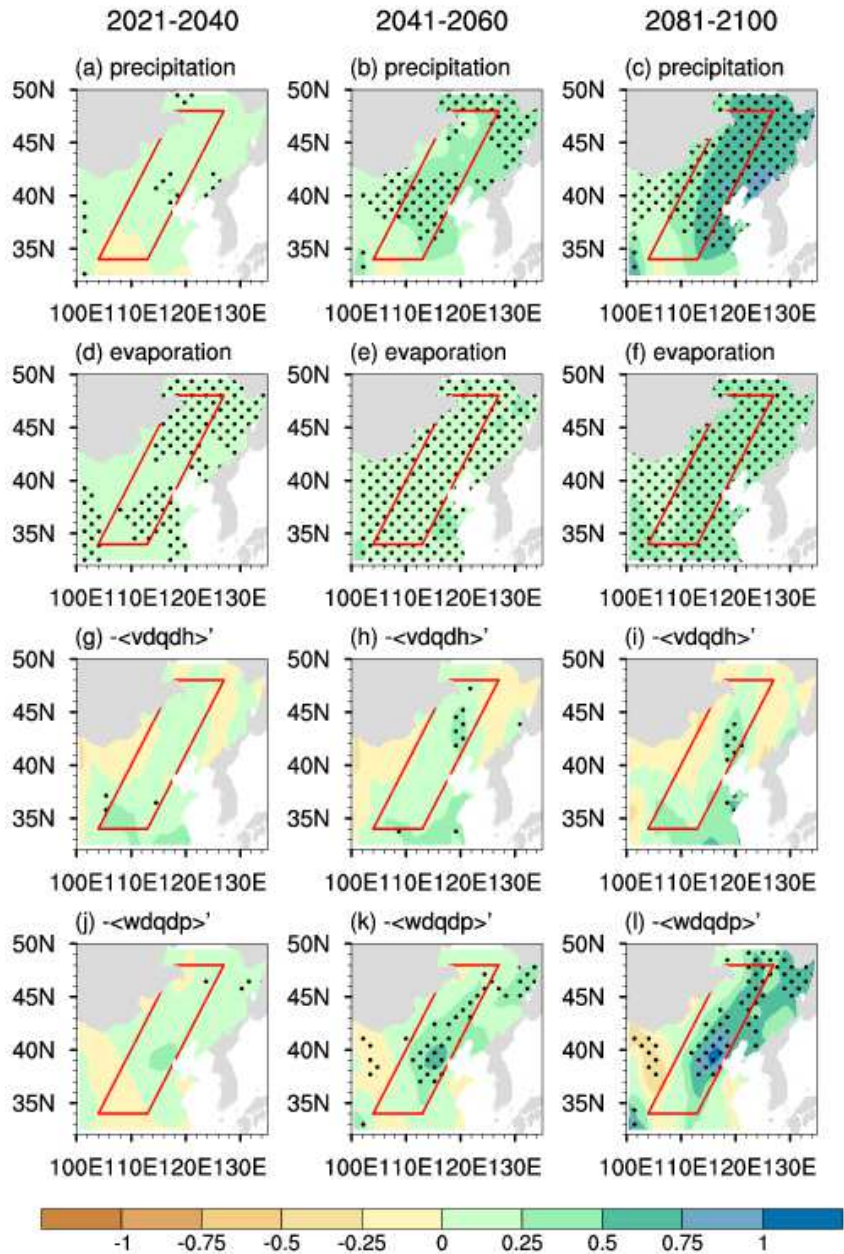
623

624

625

626

**Fig. 7.** Changes in precipitation, evaporation, horizontal moisture convergence ( $-\langle vdqdh \rangle$ ) and vertical moisture convergence ( $-\langle wdqdp \rangle$ ) in (a, b) winter, (c, d) spring, (e, f) summer and (g, h) autumn in the near-term, mid-term and long-term relative to the present-day climatology derived from the CMIP5 (left-hand panels) and CMIP6 (right-hand panels) model ensembles (units:  $\text{mm day}^{-1}$ ). Box-and-whisker plots present the 10th, 25th, 50th, 75th and 90th percentiles.



627

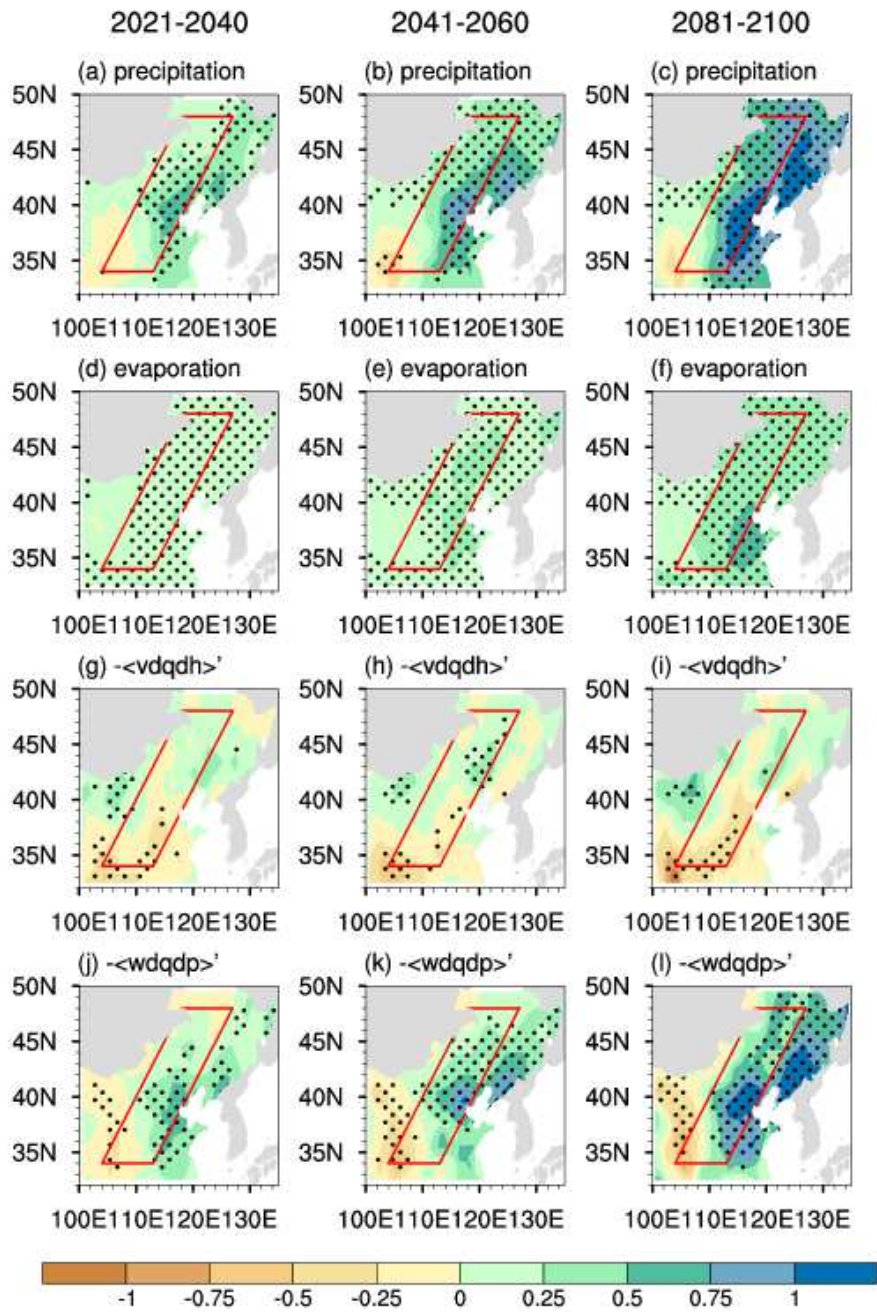
628

629

630

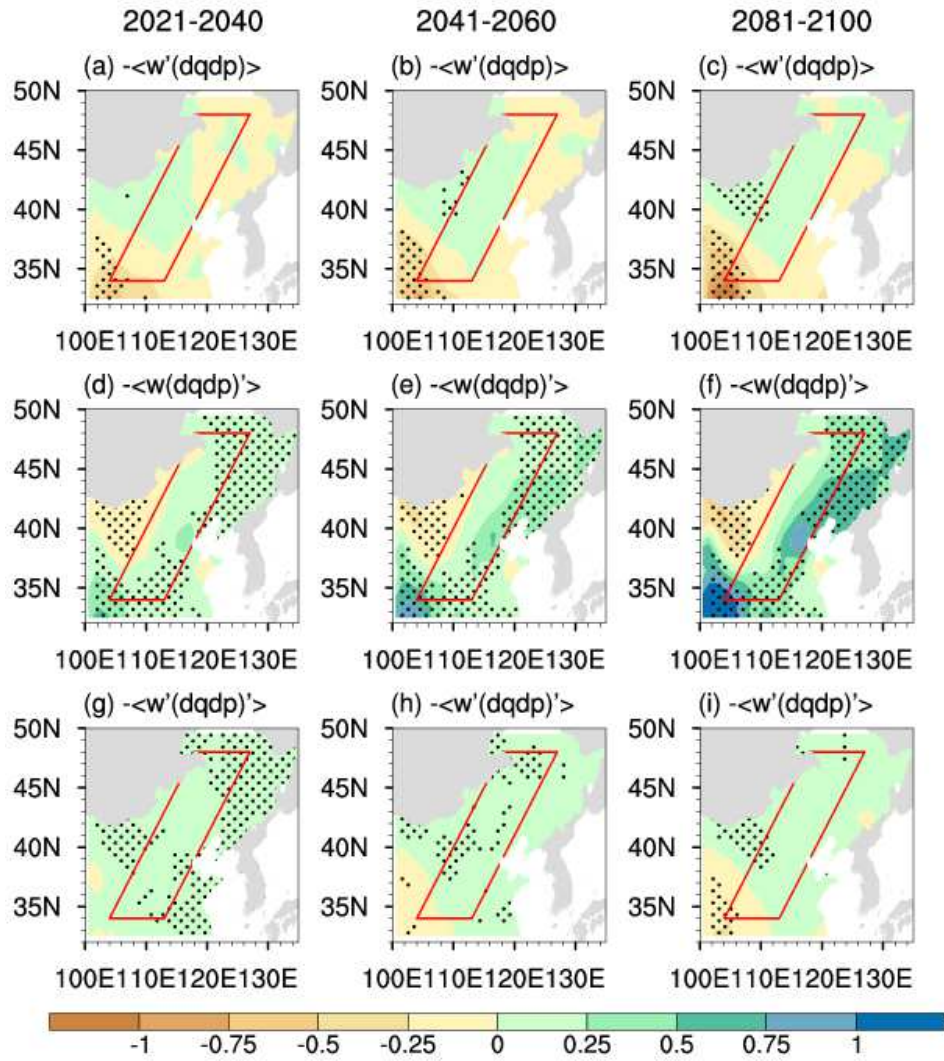
631

**Fig. 8.** Changes in precipitation, evaporation, horizontal moisture advection ( $-\langle vdqdh \rangle'$ ) and vertical moisture advection ( $-\langle wdqdp \rangle'$ ) for the MME of CMIP5 models in the near-term (left-hand panels), mid-term (middle panels) and long-term (right-hand panels) under the RCP8.5 scenario compared to the present-day climatology (unit:  $\text{mm day}^{-1}$ ). The dotted area denotes that at least three quarters of modes share the same-sign changes.



632

633 **Fig. 9.** As in Fig. 8, but for the CMIP6 MME.



634

635

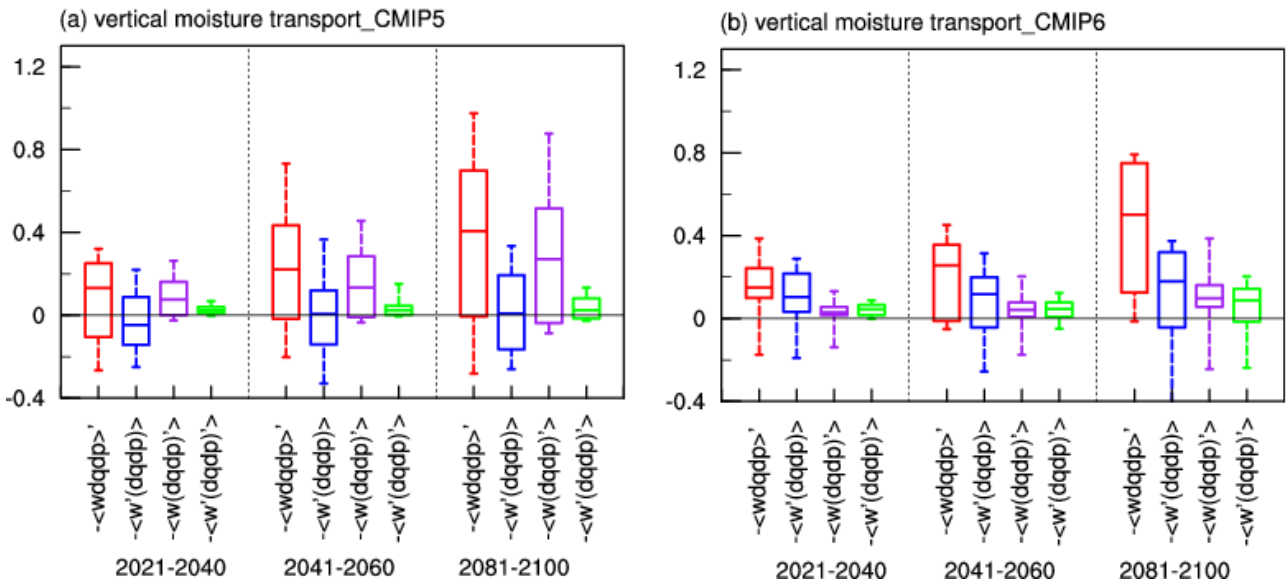
636

637

638

639

**Fig. 10.** The dynamic ( $-\langle w'(dqdp) \rangle$ ), thermodynamic ( $-\langle w(dqdp)' \rangle$ ) and nonlinear ( $-\langle w'(dqdp)' \rangle$ ) components of the changes in vertical moisture advection for CMIP5 MME in the near-term (left-hand panels), mid-term (middle panels) and long-term (right-hand panels) under the RCP8.5 scenario compared to the present-day climatology (unit:  $\text{mm day}^{-1}$ ). The dotted areas denote that at least three quarters of models share same-sign changes.



640

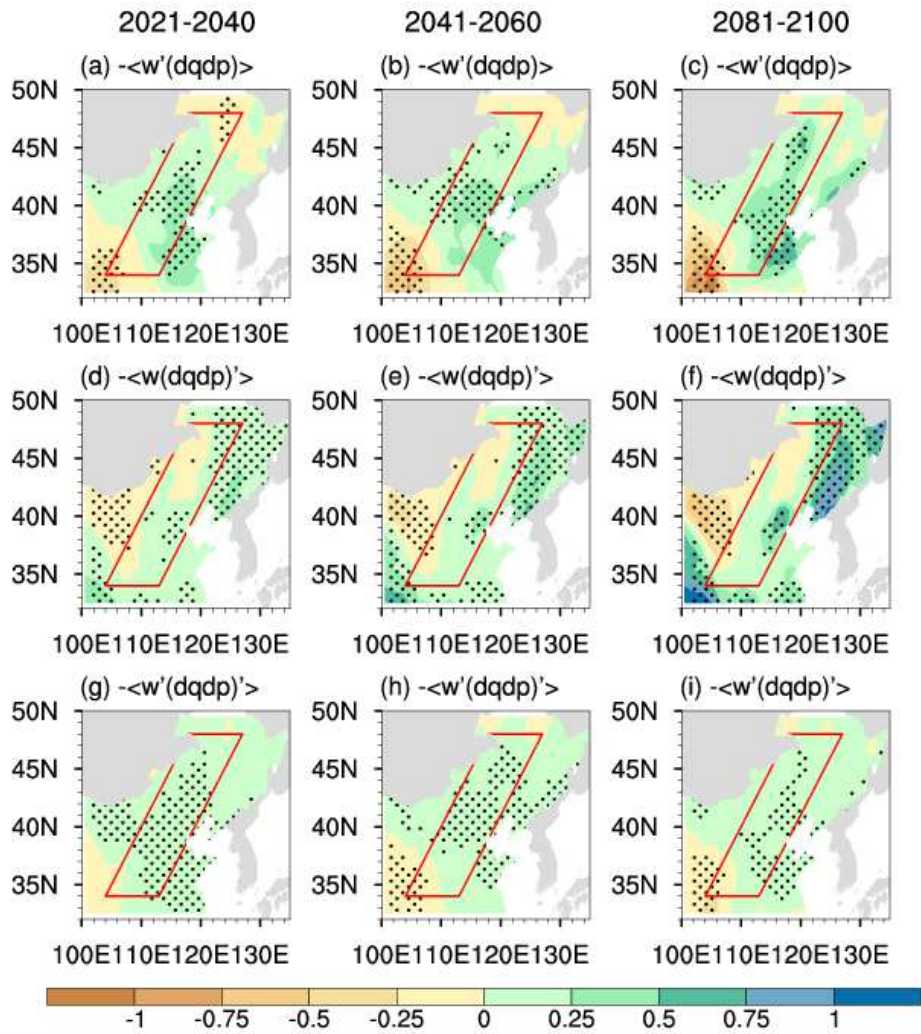
641

642

643

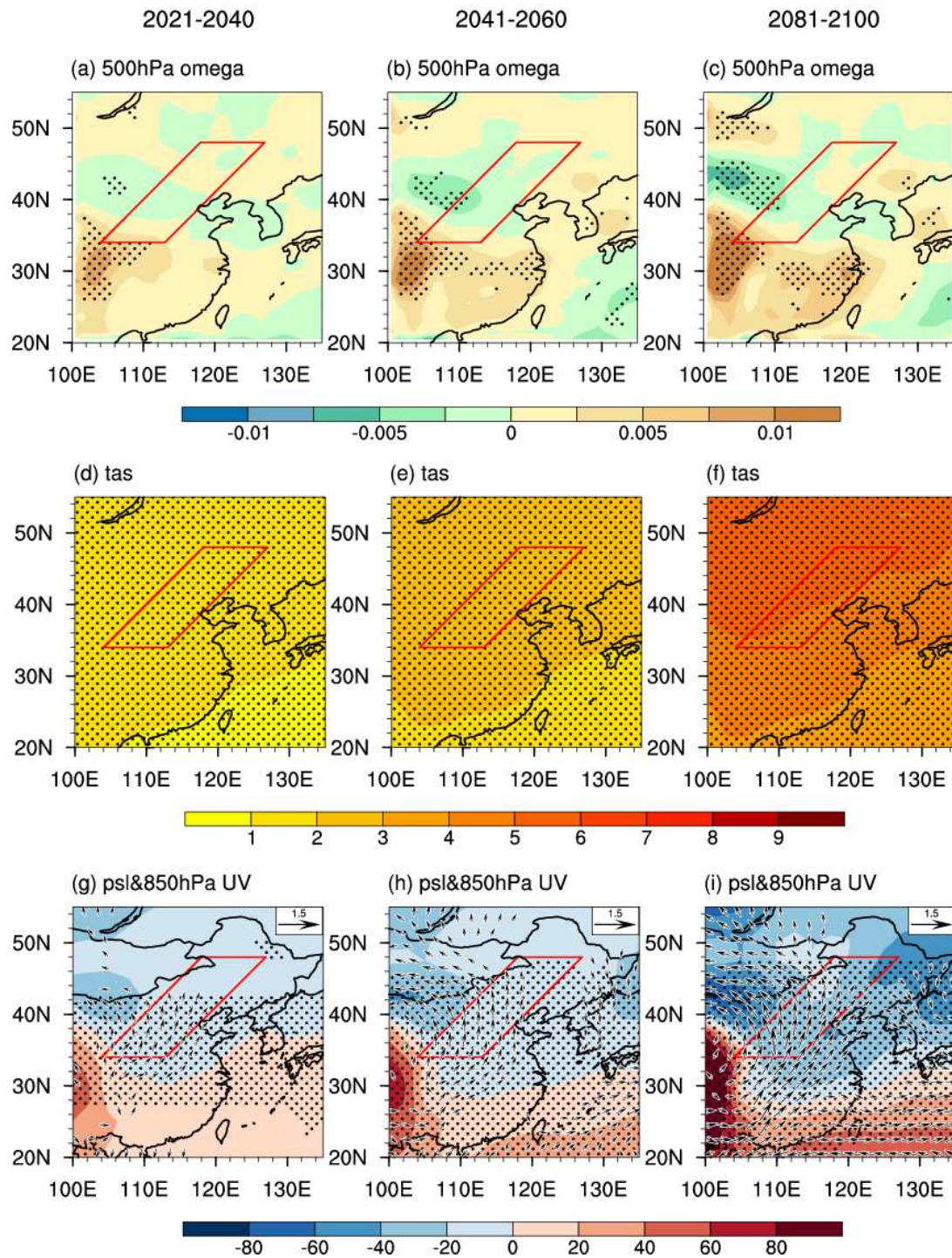
644

**Fig. 11.** Changes in vertical moisture advection ( $-\langle w dqdp \rangle'$ ) and its dynamic ( $-\langle w' dqdp \rangle'$ ), thermodynamic ( $-\langle w(dqdp) \rangle'$ ) and nonlinear ( $-\langle w'(dqdp) \rangle'$ ) components in the near-term, mid-term and long-term relative to the present-day climatology derived from the **a** CMIP5 and **b** CMIP6 model ensembles (unit:  $\text{mm day}^{-1}$ ). Box-and-whisker plots present the 10th, 25th, 50th, 75th and 90th percentiles.



645

646 **Fig. 12.** As in Fig. 10, but for the CMIP6 MME.



647

648

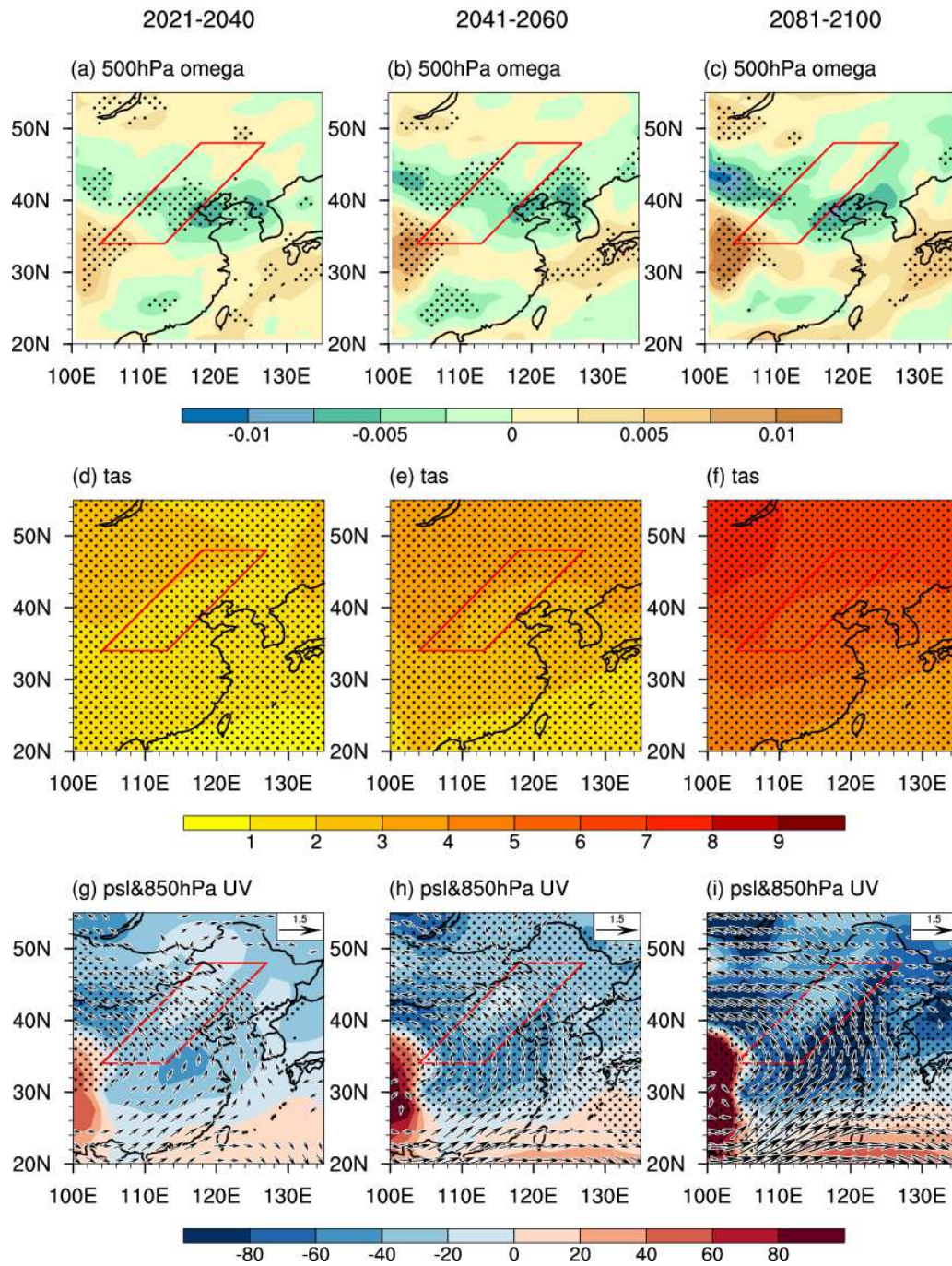
649

650

651

652

**Fig. 13.** Changes in vertical velocity at 500 hPa (unit:  $\text{Pa s}^{-1}$ ), surface air temperature (unit:  $^{\circ}\text{C}$ ), sea level pressure (unit: Pa) and horizontal wind at 850 hPa (unit:  $\text{m s}^{-1}$ ) for the CMIP5 MME in the near-term (left-hand panels), mid-term (middle panels) and long-term (right-hand panels) under the RCP8.5 scenario compared to the present-day climatology. The dotted areas denote that at least three quarters of models share same-sign changes.



653

654 **Fig. 14.** As in Fig.13, but for the CMIP6 MME.

# Figures

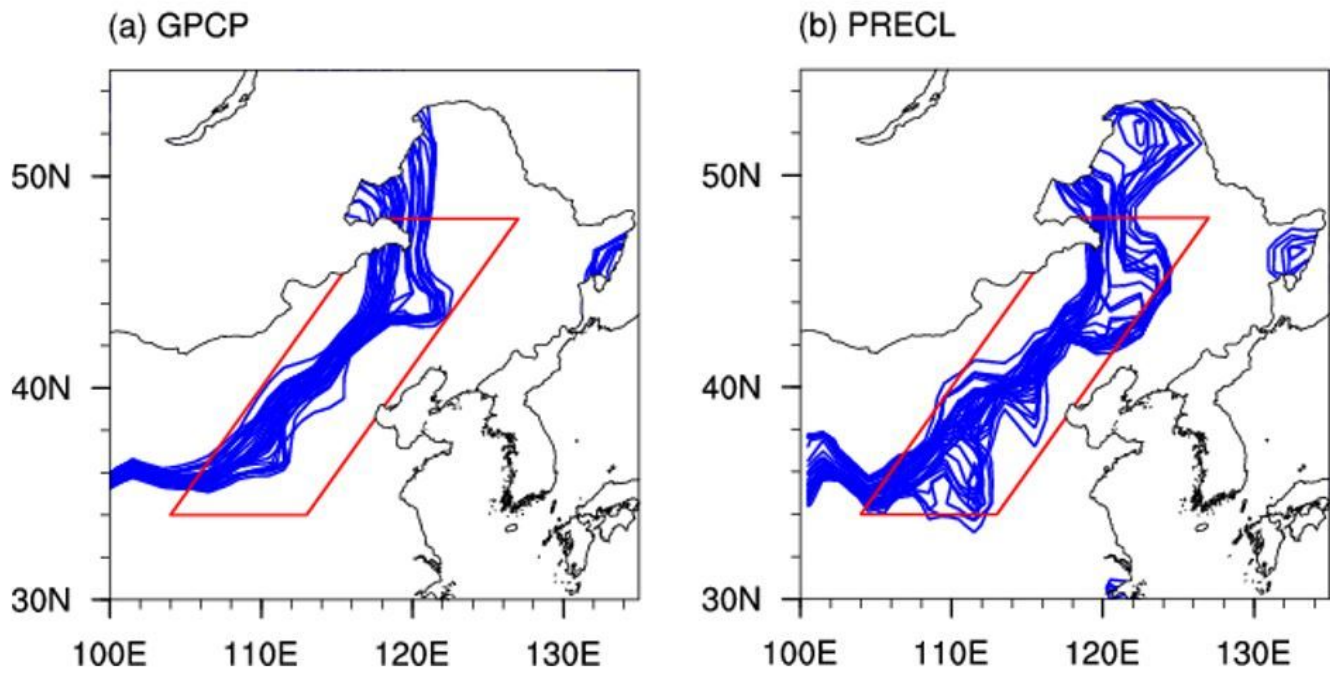


**Figure 1**

The 7-year running-mean precipitation differences equal to 2 mm day<sup>-1</sup> between boreal summer (i.e., MJJJAS-averaged) and winter (i.e., NDJFM-averaged) during 1979–2005 (blue lines). The red boxes in a and b represent the selected MTZ region.

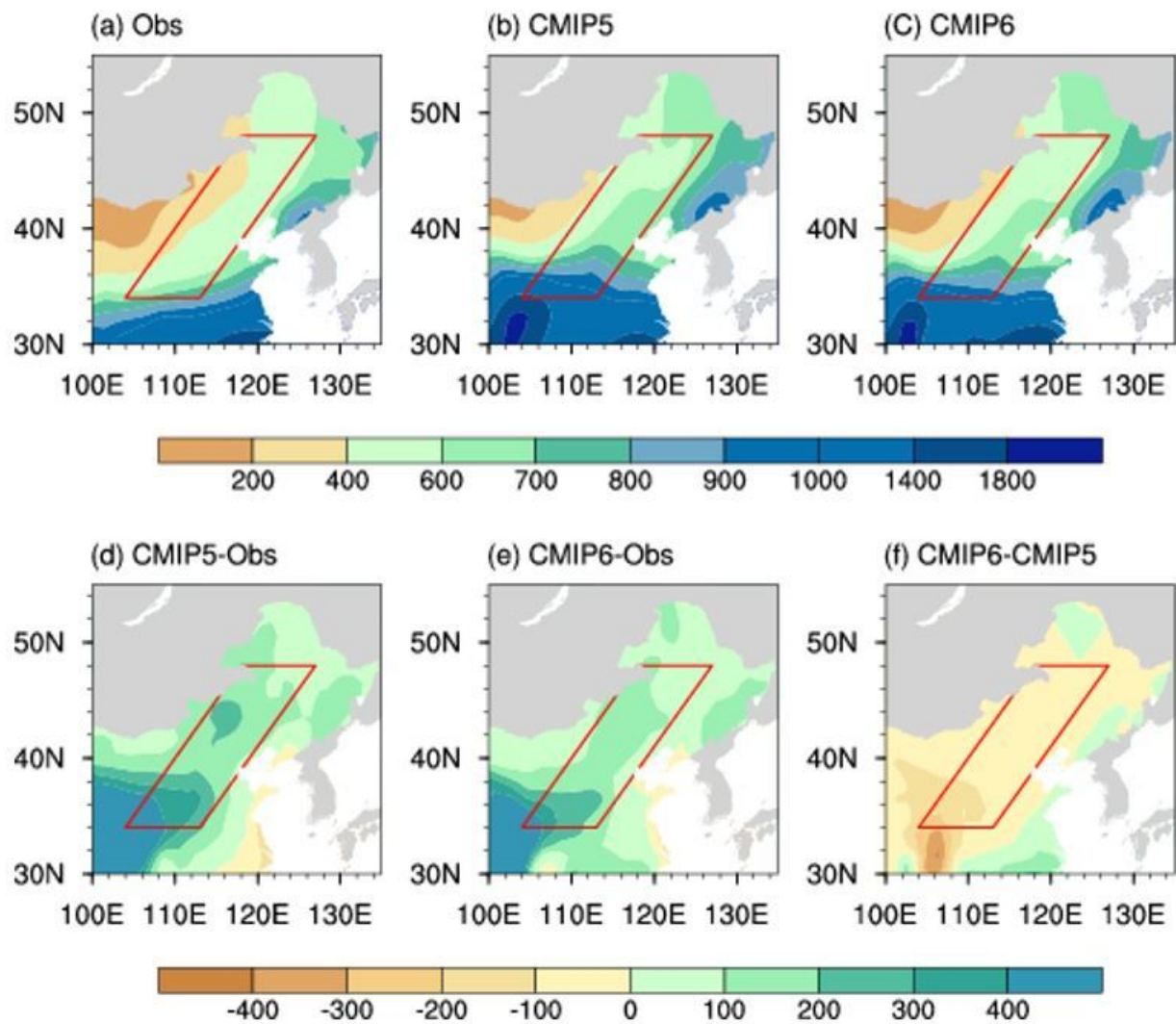


**Figure 2**

Mean annual total precipitation in the a GPCP, and the MME of b CMIP5 and c CMIP6 models over 1979–2005 (unit: mm year<sup>-1</sup>). Differences in the mean annual total precipitation between d the MME of CMIP5 and GPCP, e the MME of CMIP6 and GPCP, and f the MME of CMIP6 and CMIP5.

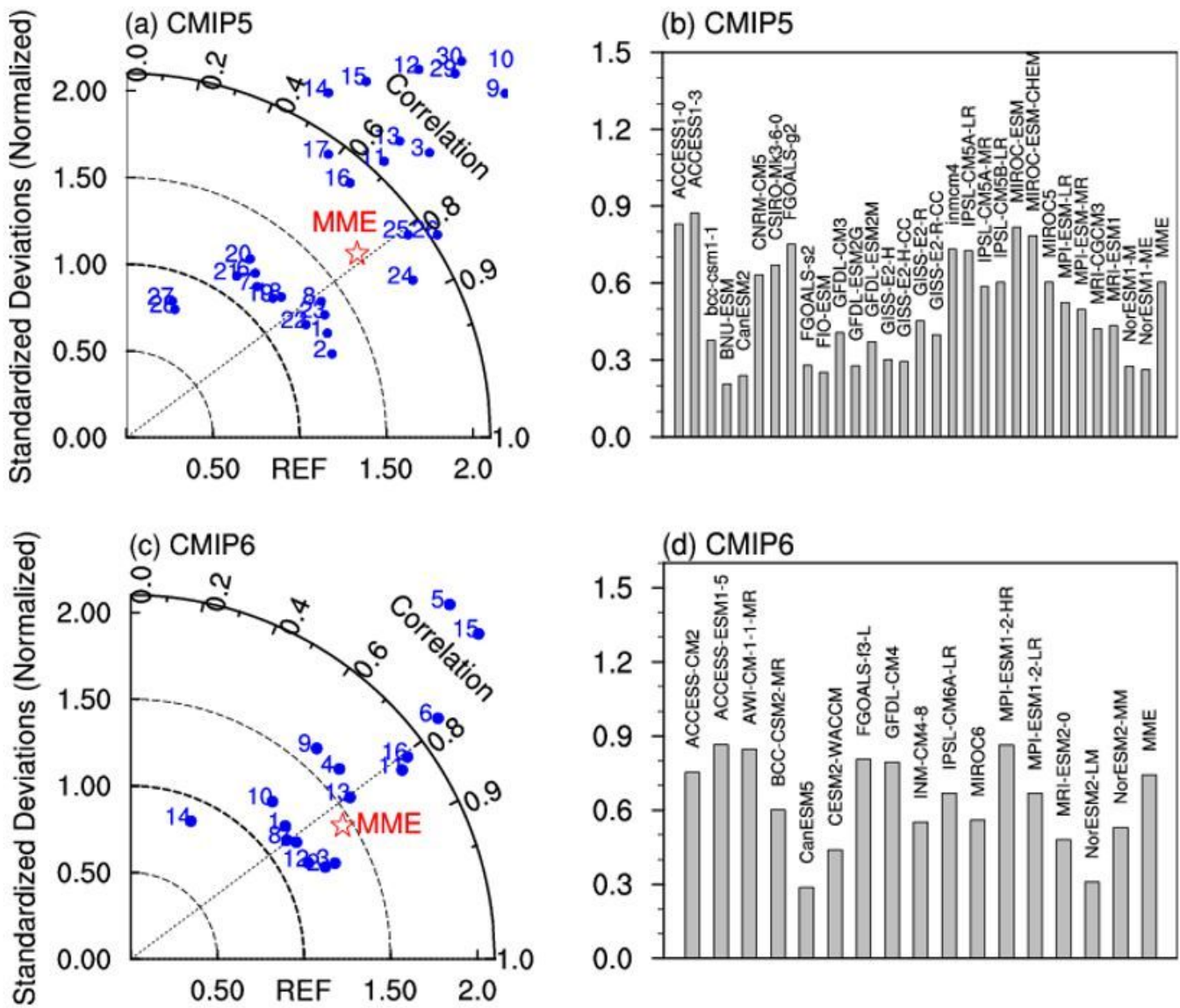
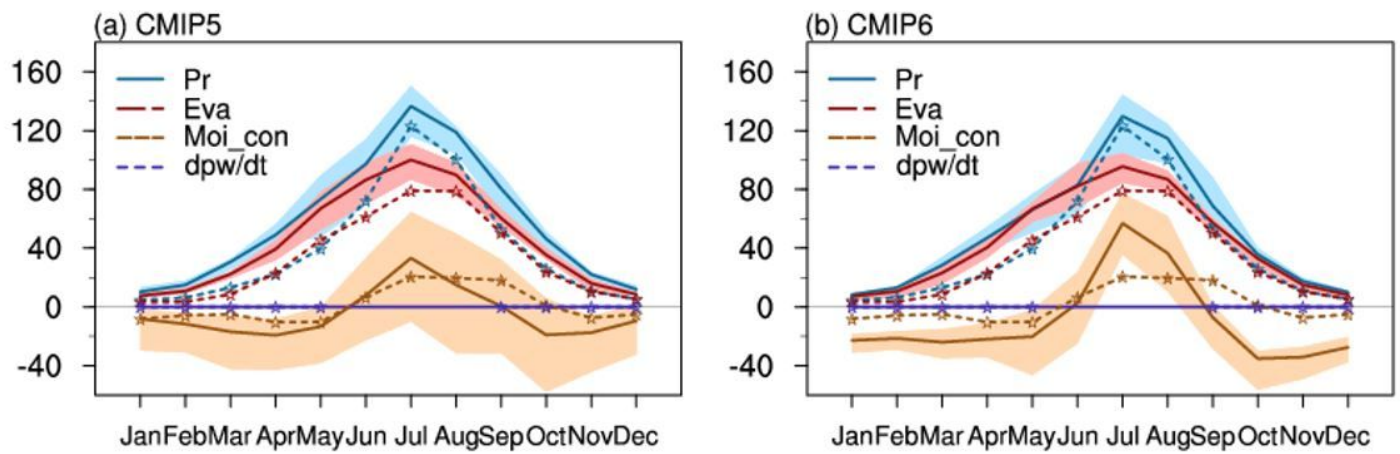


Figure 3

Taylor diagrams (left-hand panels) and skill scores (right-hand panels) of the simulated precipitation over the MTZ region for the (a, b) CMIP5 and (c, d) CMIP6 models against the observations.



**Figure 4**

The climatological mean annual cycle of precipitation (Pr), evaporation (Eva), vertically integrated moisture convergence (Moi\_con) and tendency of atmospheric precipitable water (dpw/dt) over the MTZ region obtained from ERA-Interim (lines with asterisks), the MME means (lines), and the 25th–75th percentile model intervals (shading) for the a CMIP5 and b CMIP6 ensembles (lines) (units: mm month<sup>-1</sup>).

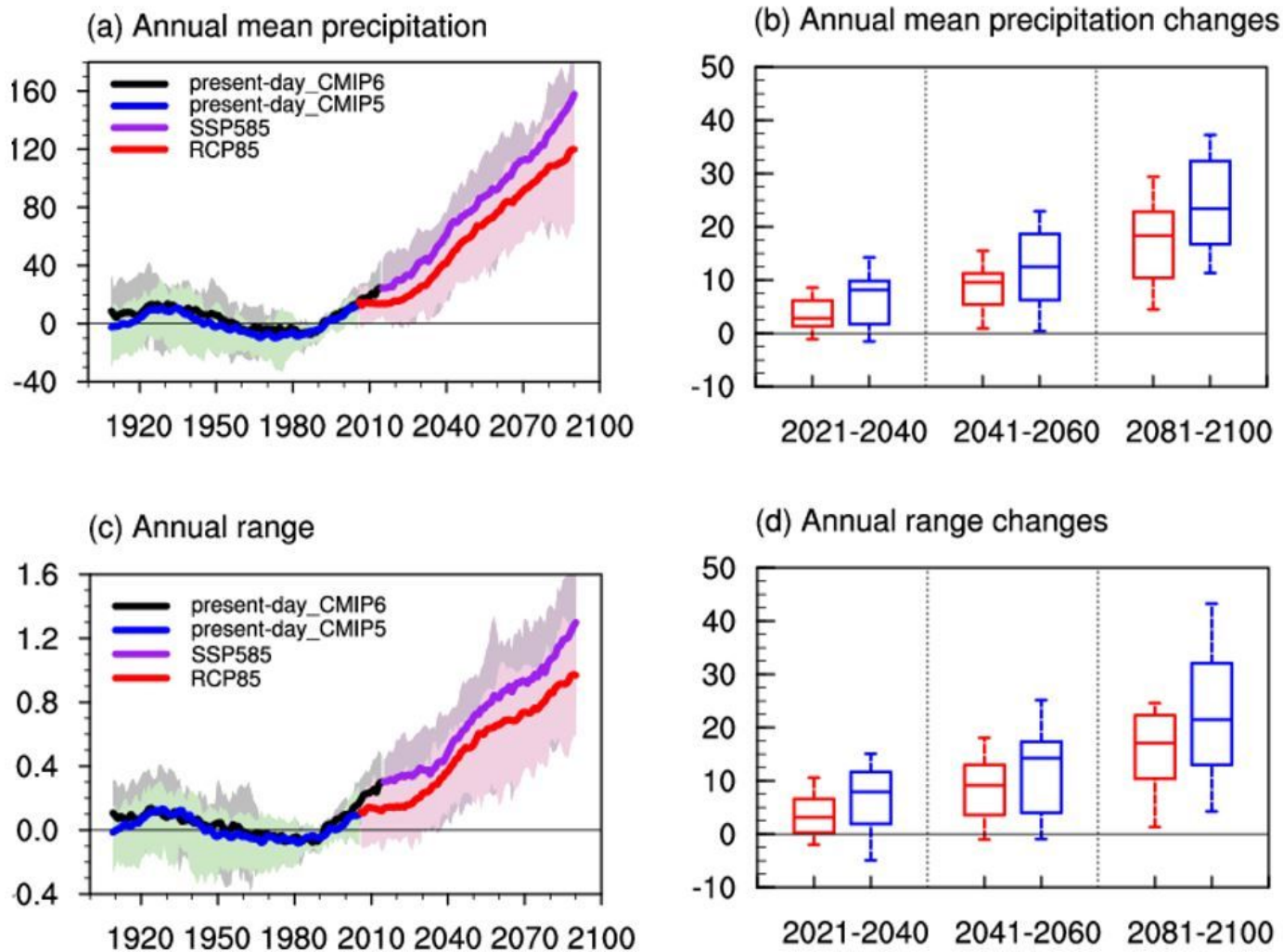


**Figure 5**

MME mean (lines) and the 25th–75th percentile model intervals (shading) for the 20-year running mean anomalies of the a annual total precipitation (unit: mm year<sup>-1</sup>) and c the annual precipitation range (unit: mm day<sup>-1</sup>) relative to the present-day climatology (1979–2005) over the MTZ region. Changes in the b annual total precipitation and d annual precipitation range (%) for the near-term (2021–2040), mid-term (2041–2060) and long-term (2081–2100) relative to the present-day (1979–2005) climatology for the CMIP5 (red) and CMIP6 (blue) ensembles. Box-and-whisker plots present the 10th, 25th, 50th, 75th and 90th percentiles.

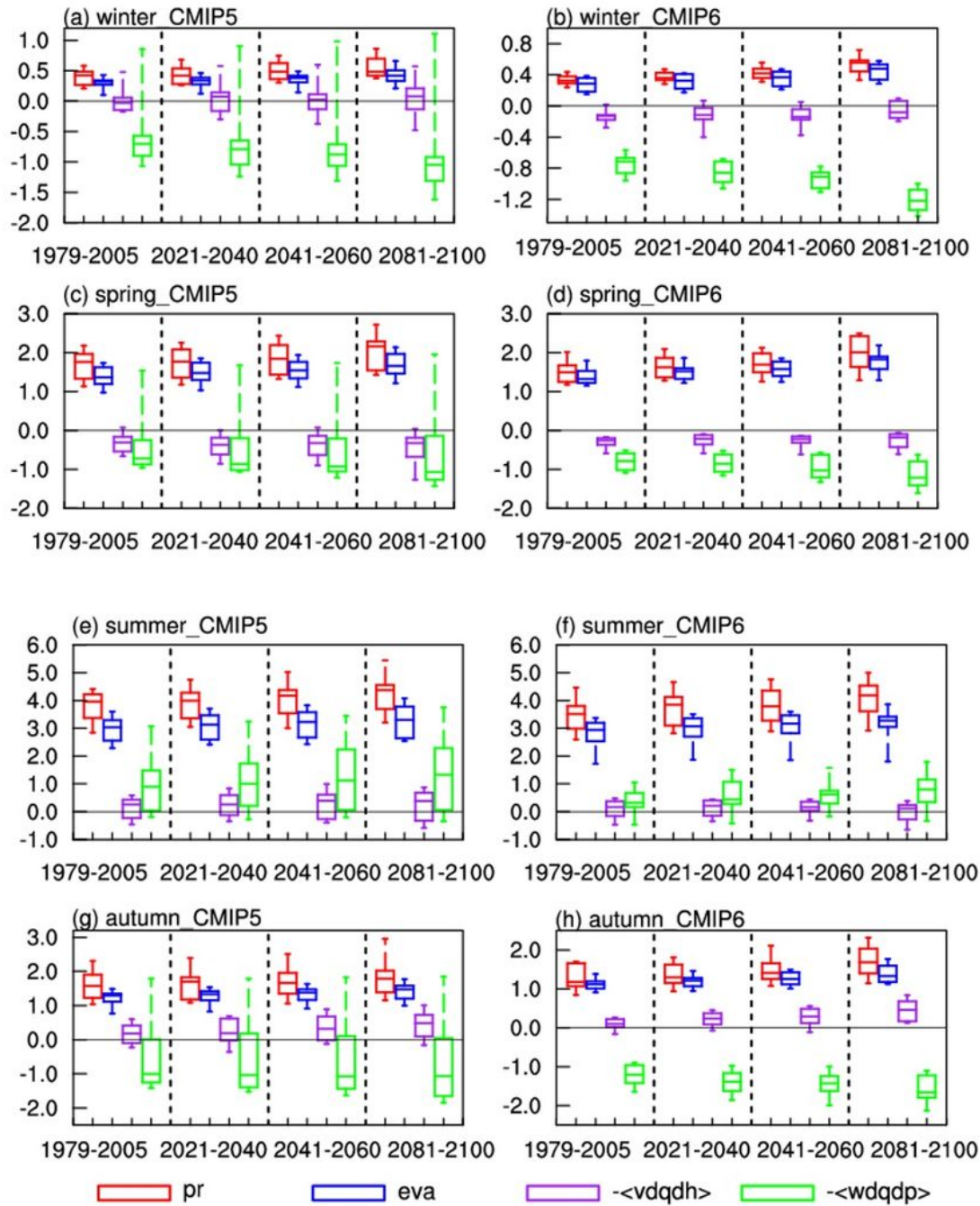


**Figure 6**

Climatological mean amount of precipitation, evaporation, horizontal moisture advection ( $-$ ) and vertical moisture advection ( $-$ ) in (a, b) winter, (c, d) spring, (e, f) summer and (g, h) autumn, for the present-day, near-term, mid-term and long-term derived from the CMIP5 (left-hand panels) and CMIP6 (right-hand panels) model ensembles (units:  $\text{mm day}^{-1}$ ). Box-and-whisker plots present the 10th, 25th, 50th, 75th and 90th percentiles.

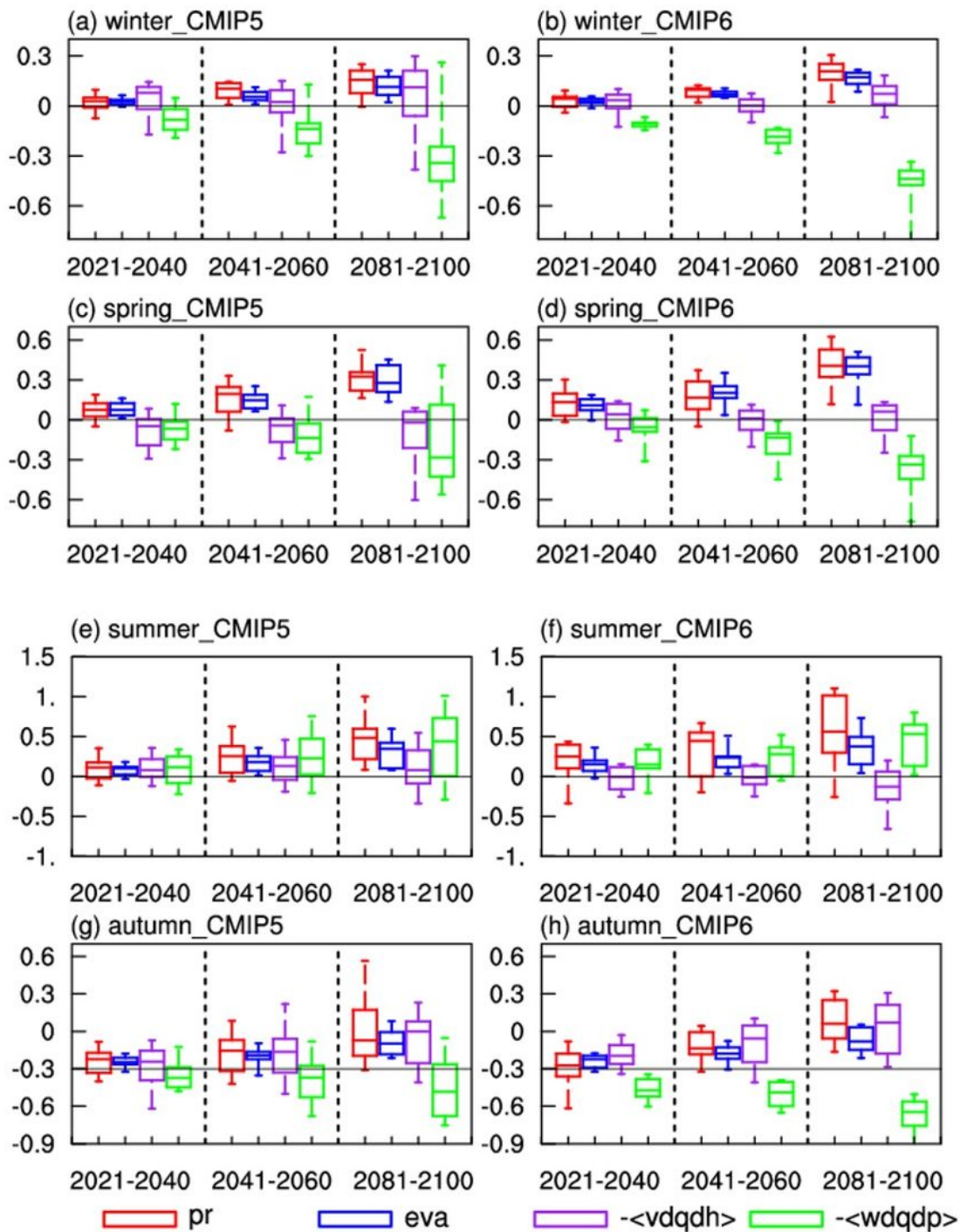


**Figure 7**

Changes in precipitation, evaporation, horizontal moisture convergence (-) and vertical moisture convergence (-) in (a, b) winter, (c, d) spring, (e, f) summer and (g, h) autumn in the near-term, mid-term and long-term relative to the present-day climatology derived from the CMIP5 (left-hand panels) and CMIP6 (right-hand panels) model ensembles (units: mm day<sup>-1</sup>). Box-and-whisker plots present the 10th, 25th, 50th, 75th and 90th percentiles.

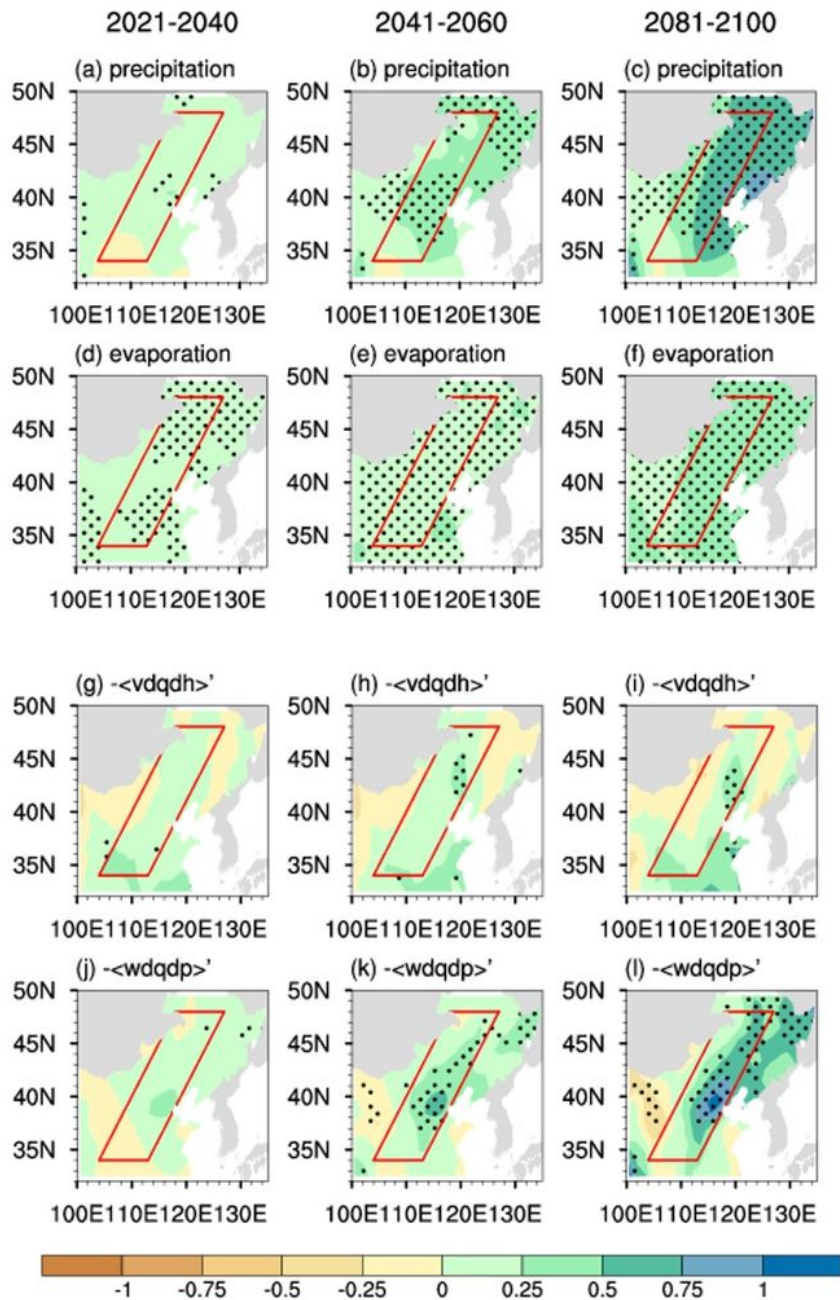


**Figure 8**

Changes in precipitation, evaporation, horizontal moisture advection ( $-\langle vdqdh \rangle$ ) and vertical moisture advection ( $-\langle wdqdp \rangle$ ) for the MME of CMIP5 models in the near-term (left-hand panels), mid-term (middle panels) and long-term (right-hand panels) under the RCP8.5 scenario compared to the present-day climatology (unit: mm day<sup>-1</sup>). The dotted area denotes that at least three quarters of modes share the same-sign changes.

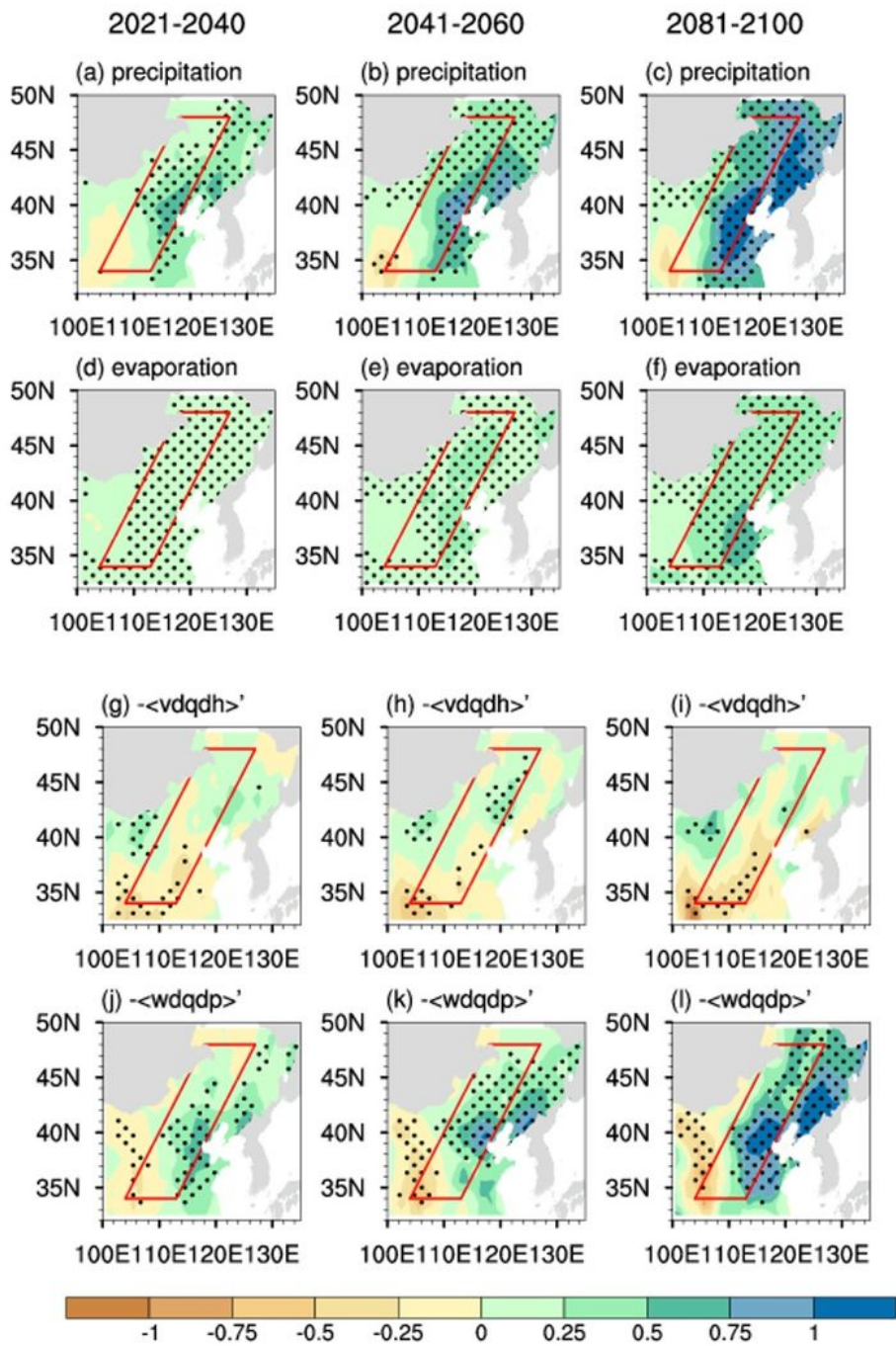


**Figure 9**

As in Fig. 8, but for the CMIP6 MME.

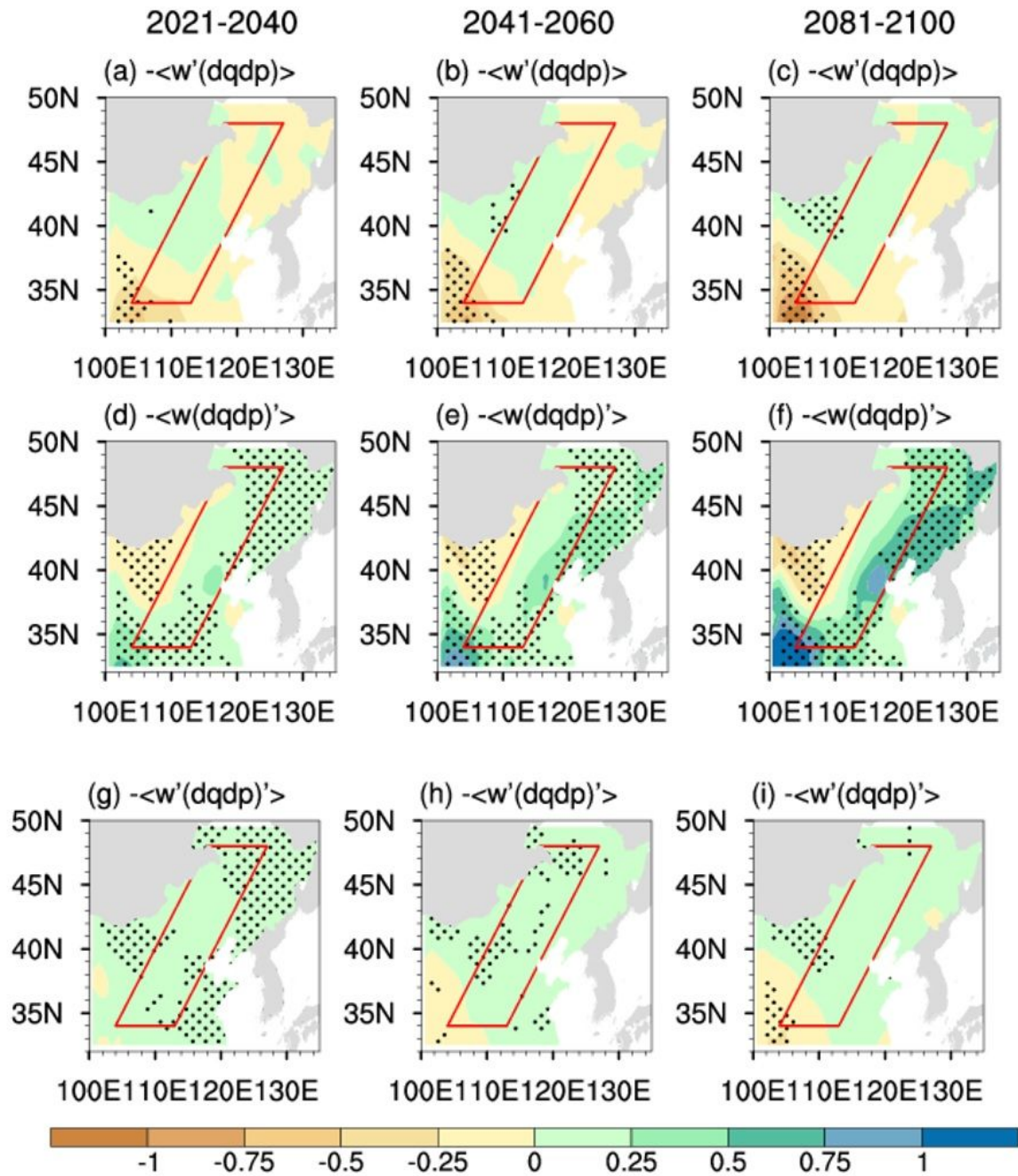


**Figure 10**

The dynamic (-), thermodynamic (-) and nonlinear (-) components of the changes in vertical moisture advection for CMIP5 MME in the near-term (left-hand panels), mid-term (middle panels) and long-term (right-hand panels) under the RCP8.5 scenario compared to the present-day climatology (unit:  $\text{mm day}^{-1}$ ). The dotted areas denote that at least three quarters of models share same-sign changes.

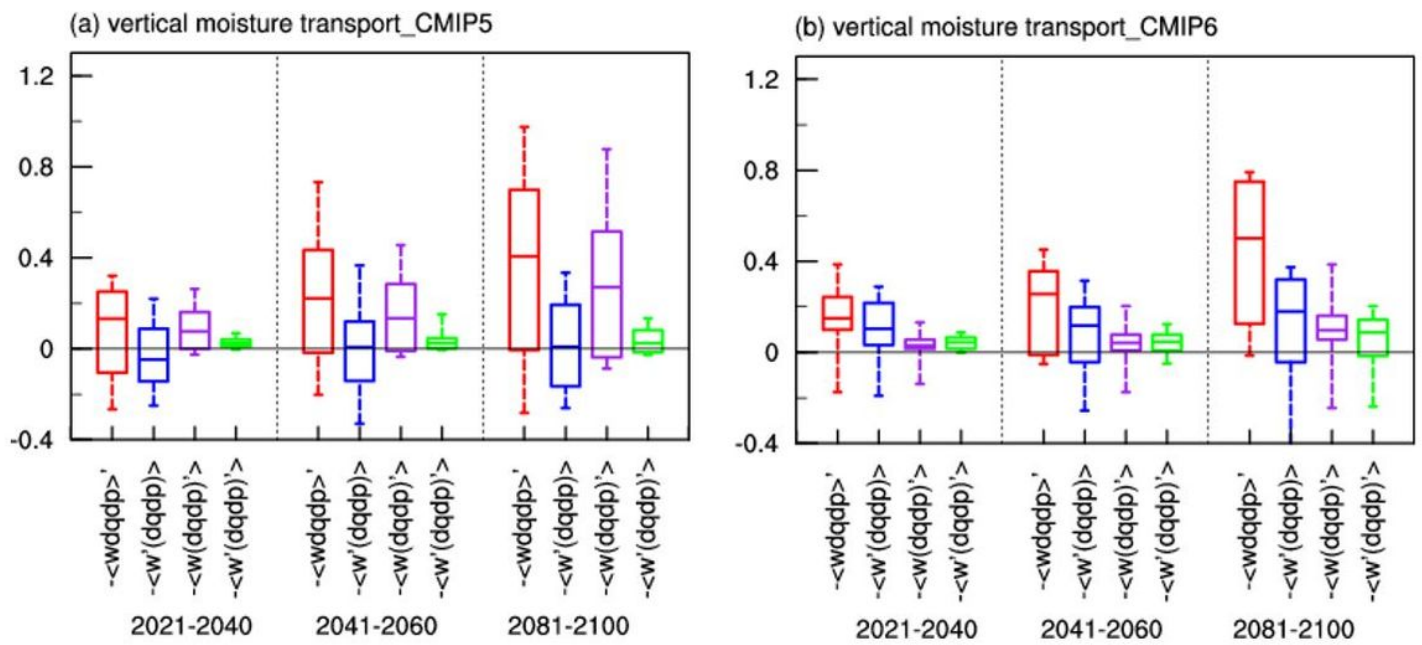


**Figure 11**

Changes in vertical moisture advection ( $\bar{w}$ ) and its dynamic ( $\bar{w}'$ ), thermodynamic ( $\bar{w}''$ ) and nonlinear ( $\bar{w}'''$ ) components in the near-term, mid-term and long-term relative to the present-day climatology derived from the a) CMIP5 and b) CMIP6 model ensembles (unit: mm day<sup>-1</sup>). Box-and-whisker plots present the 10th, 25th, 50th, 75th and 90th percentiles.

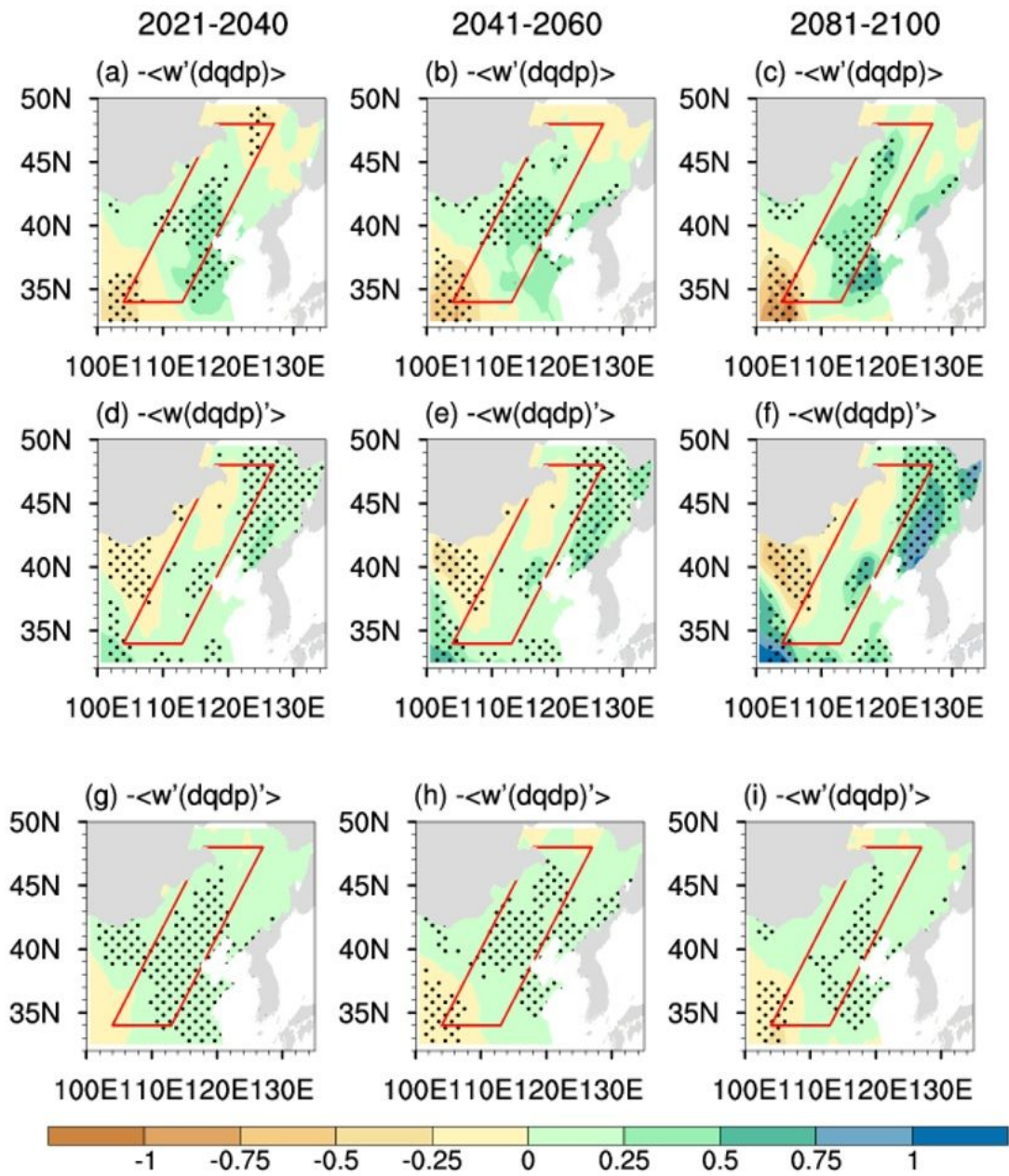
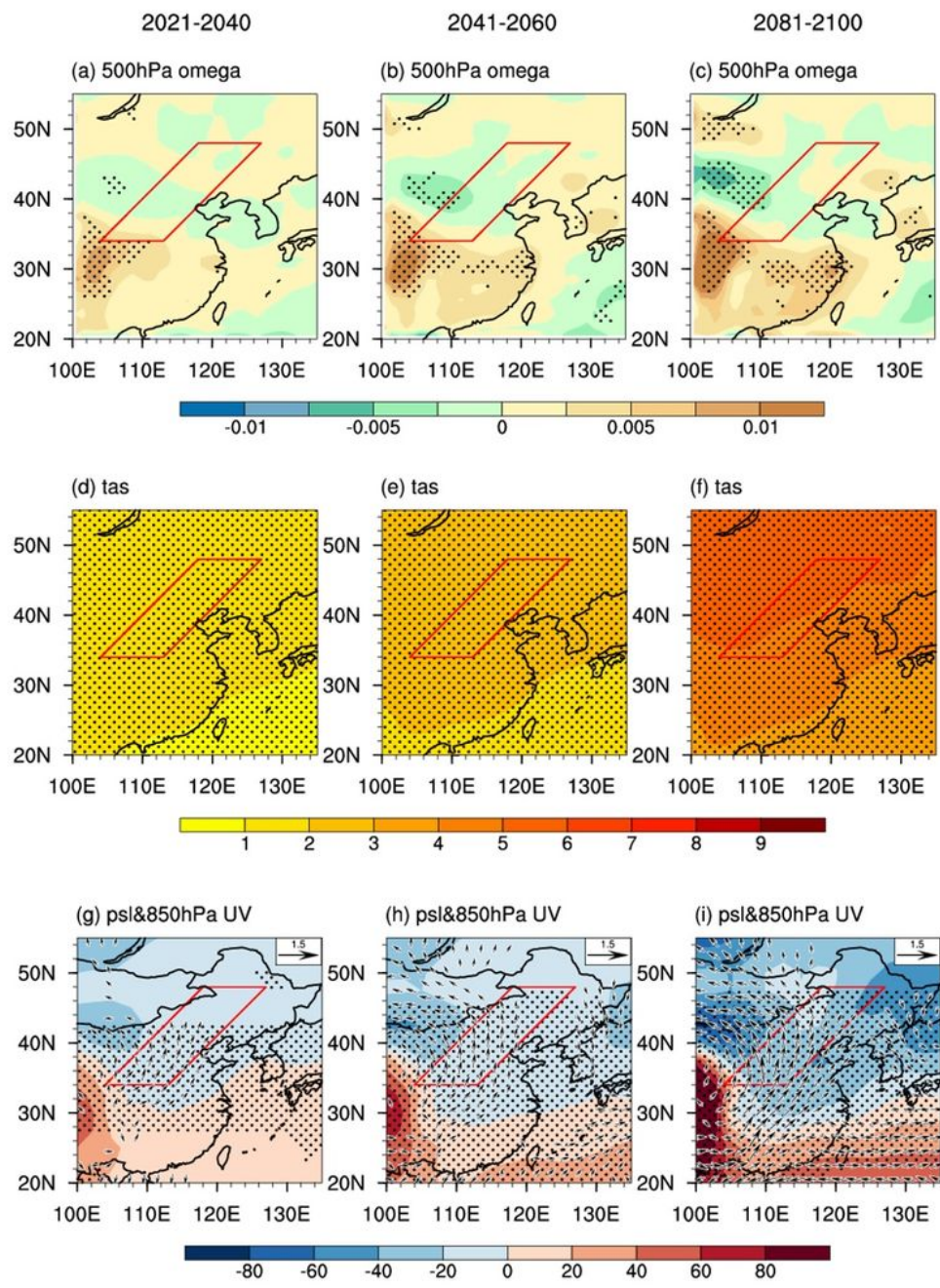


Figure 12

As in Fig. 10, but for the CMIP6 MME.



**Figure 13**

Changes in vertical velocity at 500 hPa (unit: Pa s<sup>-1</sup>), surface air temperature (unit: K), sea level pressure (unit: Pa) and horizontal wind at 850 hPa (unit: m s<sup>-1</sup>) for the CMIP5 MME in the near-term (left-hand panels), mid-term (middle panels) and long-term (right-hand panels) under the RCP8.5 scenario compared to the present-day climatology. The dotted areas denote that at least three quarters of models share same-sign changes.

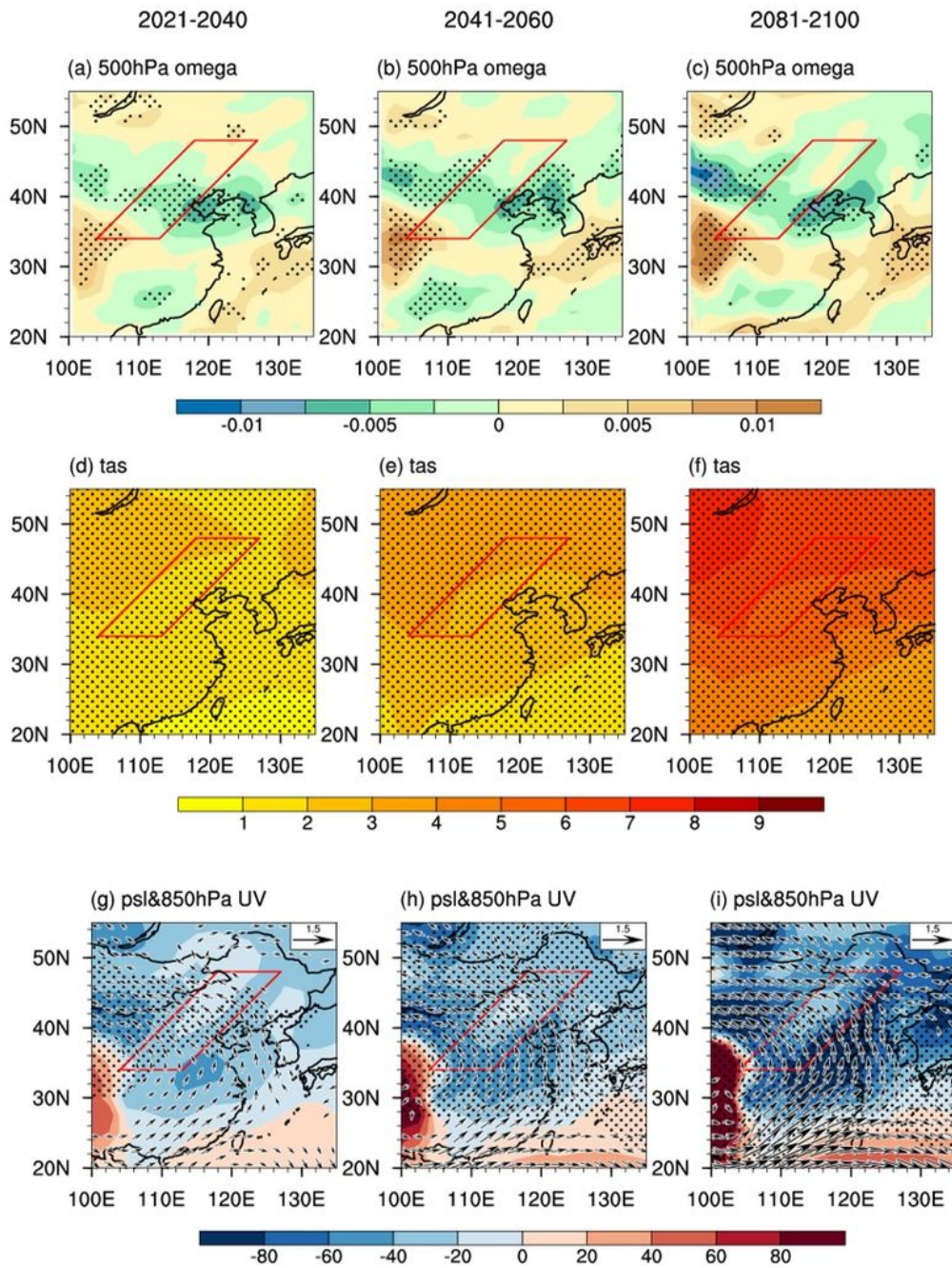


**Figure 14**

As in Fig.13, but for the CMIP6 MME.